JGR Solid Earth

RESEARCH ARTICLE

10.1029/2022JB024070

Special Section:
Heterogeneity, anisotropy and scale-dependency: Keys to understand Earth composition, structure and behavior

Key Points:

- We combine separate geophone deployments with broadband data using ambient noise and beamforming to measure H/V ratios and phase velocity
- A low velocity zone likely exists at approximately 10 km depth coinciding with areas of high surface heat flux and geothermal activity
- We find strong similarities between the geothermal region in Utah and the Coso geothermal field

Correspondence to:
D. Wells,
u0770911@utah.edu;
danedwells@gmail.com

Citation:
Wells, D., Lin, F.-C., Pankow, K., Baker, B., & Bartley, J. (2022). Combining dense seismic arrays and broadband data to image the subsurface velocity structure in geothermally active south-central Utah. *Journal of Geophysical Research: Solid Earth*, *127*, e2022JB024070. https://doi.org/10.1029/2022JB024070

Received 19 JAN 2022
Accepted 11 JUN 2022

Combining Dense Seismic Arrays and Broadband Data to Image the Subsurface Velocity Structure in Geothermally Active South-Central Utah

Daniel Wells[1], Fan-Chi Lin[1], Kristine Pankow[1], Ben Baker[1], and John Bartley[1]

[1]University of Utah, Salt Lake City, UT, USA

Abstract South-central Utah is characterized by Quaternary volcanism, current geothermal activity, and unusually high surface heat flux across the region. Additionally, there are three operating geothermal power plants in this region, known as the Sevier thermal area. This setting is very similar to that found in the Coso geothermal area. However, the source and lateral extent of subsurface heat in Utah is poorly understood. We use temporally separated geophone arrays combined with regional broadband data to perform ambient noise seismic tomography to study the subsurface shear velocity structure in the region. We find good recovery of ocean-seism excited Rayleigh wave signals between the periods of 5 and 10 s. For each period, we measure the Rayleigh wave phase velocity and ellipticity across the region using the beamforming methodology and horizontal to vertical (H/V) amplitude ratio. Finally, we combine spline-based 1D shear velocity models inverted using Rayleigh wave phase velocity and H/V measurements on a 2D, beamforming discretized grid to construct a final 3D model. The final 3D model has many similarities to imaged velocity models at the Coso geothermal area. We find a strong correlation between low velocity anomalies and high surface heat flux and geothermal activity. Additionally, we find a laterally continuous low-velocity anomaly between 5 and 15 km depth, which may represent elevated temperature of hundreds of degrees Celsius, partial melt, and/or the presence of water, and a common heat source across the region which likely originates from the mantle.

Plain Language Summary South-central Utah is a geologically interesting area, featuring recent volcanism and surface hydrothermal features and has measurably high surface heat flux, similar to the Coso geothermal resource area in California. However, the source of heat driving these features in Utah is poorly understood. To investigate, we use four temporally separate portable seismometer (geophone) arrays that record seismic waves for a duration of 1 month each, and we mathematically correlate the wavefield between all of these geophones with 30 permanent, broadband seismometers in the region. We find the strongest signal in Rayleigh surface waves originating from ocean waves on the coast. We use a measurement technique called beamforming to measure the velocity at which these waves propagate across the arrays, and we measure the ratios of the horizontal wave amplitudes to the vertical amplitudes. These measurements are used together to estimate a 3D shear wave velocity model between 0 and 15 km depth. We find a low shear velocity layer at 10 km depth, with the lowest velocity areas coinciding with the high surface heat flow and geothermal areas, indicating potential for elevated temperature, weaker crust and continuity of heat source across the region, likely stemming from the mantle.

1. Introduction

The Basin and Range in the western US is a physiographic region generally characterized by high heat flow (Blackwell et al., 1991). For this reason, the area has been, and continues to be, exploited for geothermal resources. In the Nevada Basin and Range, there were 25 operational geothermal power plants in 2020 that possessed a nominal combined capacity of more than 800 MW (Nevada Department of Minerals, 2021). On the western edge of the Basin and Range, in the extremely seismically active Eastern California Shear Zone (Bhattacharyya & Lees, 2002; McClusky et al., 2001) is one of the largest geothermal producing regions in the US, the Coso geothermal field (Coso Operating Company, 2021; Monastero, 2002). Coso has operating geothermal power plants, producing up to 250 MW, and surface hydrothermal features such as fumaroles, as well as Quaternary volcanism and hot, plutonic basement rock (Bacon et al., 1982; Duffield et al., 1980; Monastero et al., 2005).

South-central Utah, on the eastern edge of the Basin and Range, is in a different tectonic setting than Coso. The region is characterized by minimal seismic activity (Arabasz et al., 2007; Kreemer et al., 2012; Mesimeri, Pankow,

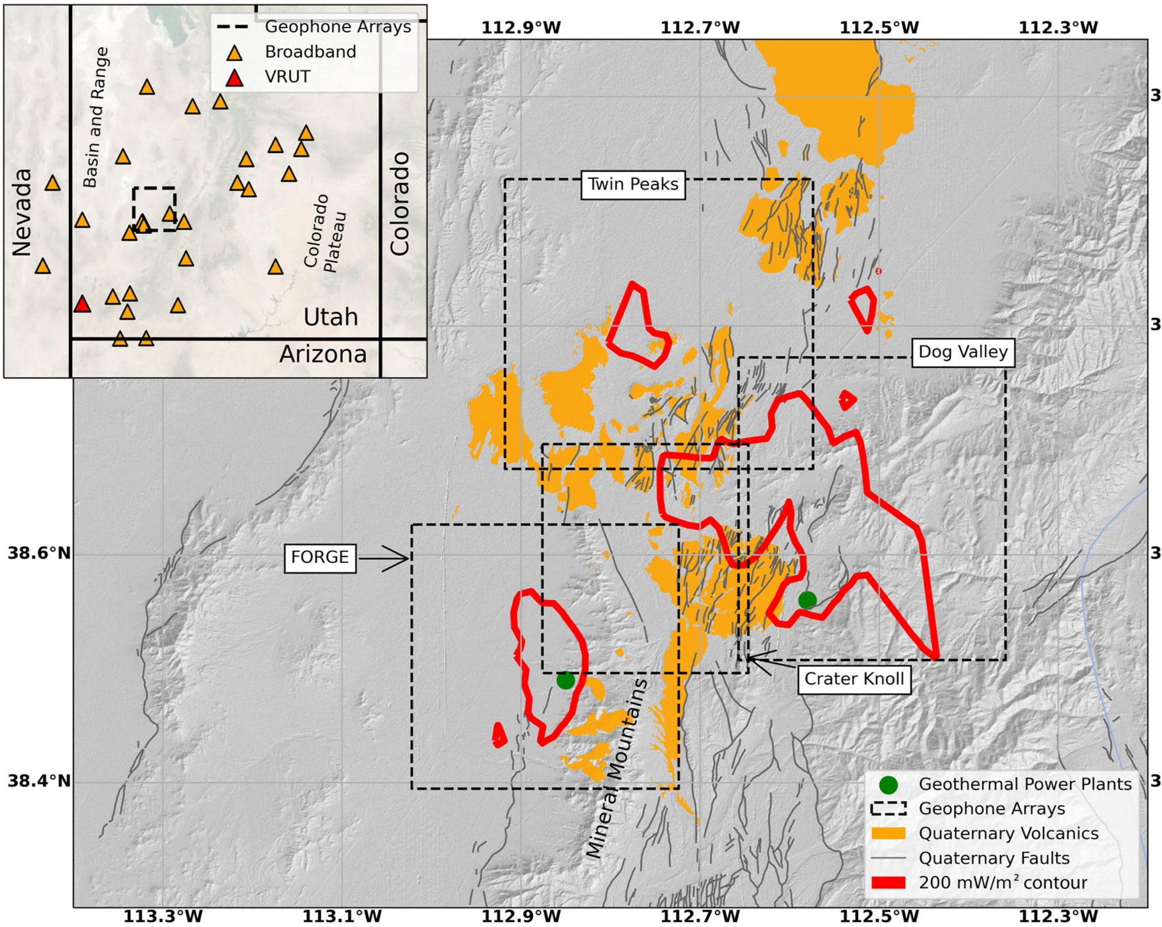

Figure 1. Study region located in south-central Utah. The locations of the four nodal geophone arrays are shown and labeled. Existing geothermal power plants, mapped Quaternary volcanics (Utah Geological Survey), Quaternary faults (Utah Geological Survey), and surface heat flux contour (Utah Geological Survey) are also shown. The Mineral Mountains are labeled and discussed in this study. Inset: location of all broadband seismometers used in the study, with the combined area of all four nodal arrays outlined in black. VRUT is used as an example virtual source in later figures.

Baker, & Hale, 2021) and a unique combination of geologic features that are relatively poorly constrained. Some of these features are similar to those found in Coso: some areas have hot, solid granitic bodies as basement rock (Moore et al., 2020) and the region has measurably higher surface heat flux than surrounding regions (Blackwell et al., 2011; Edwards & Chapman, 2013). There are also multiple active hot springs and sources of geothermal heat on the surface (Hardwick et al., 2018), as well as a series of mapped Pliocene to Quaternary volcanic deposits indicating geologically young volcanism, from 6 Ma to present, but concentrated in the last 2.5 Ma (Johnsen et al., 2010; Rowley et al., 2013; Sine et al., 2008). As a result, the greater region is classified as the Sevier geothermal resource area (Hardwick et al., 2018; Olson & Smith, 1976; Rowley et al., 2013). As at Coso, there are active geothermal power plants coincident with the locations of the higher heat flux (Figure 1).

The Sevier geothermal resource area lies largely within the Transition Zone (TZ) between the eastern edge of the Basin and Range mountainous topography and the bordering higher elevation Colorado Plateau found to the east in central Utah (Figure 1). Given the study area's location in the TZ, it has been proposed that the shallower elevated geotherm may be connected to deeper (lower crust and upper mantle), magma-source fluids associated with the boundary between thin, extending Basin and Range lithosphere and the more brittle, thicker Colorado Plateau lithosphere (Wannamaker et al., 2001, 2008).

Previous seismic studies in south-central Utah find a number of anomalies suggestive of elevated temperatures, partial melt, and/or interconnected pore fluid at crustal depths at both local and regional scale. Early seismic imaging and profiling indicates the presence of a crustal low velocity anomaly. Muller and Mueller (1979) and Keller et al. (1975) inferred a low velocity zone (LVZ) near ∼10 km depth that may extend across much of the Basin and Range geographic province, but little constraint was obtained regarding the LVZ thickness and magnitude of velocity reduction. Robinson and Iyer (1981) performed a teleseismic P-wave study and observed evidence of a localized low velocity anomaly beneath the Mineral Mountains that could be related to a subsurface source of elevated heat. This structure was imaged from ∼5 km depth to at least as far as the uppermost mantle, and is characterized by a 5%–7% velocity decrease compared to the surrounding region in the same depth range.

At a more regional scale, tomographic work incorporating data from LA RISTRA, a linear broadband seismic array that cut across southern Utah, New Mexico, and Western Texas, and the EarthScope USArray Transportable Array (TA) shows evidence of low-velocity anomalies in both the crust and upper mantle. A joint inversion for shear velocity, using Rayleigh wave phase velocity data from the TA, P-wave receiver functions from TA and LA RISTRA data, and Bouguer gravity anomaly data reveal a relatively thin crust, and relatively low shear velocity to depths of up to 50 km, with anomalies in some areas persisting to depths beyond 100 km (Bailey et al., 2012). Teleseismic body wave tomography across the LA RISTRA array reveals significant, large-scale shear velocity anomalies in the mantle and lower crust beneath the Utah portion of the deployment that persist to depths of 250 km, with perturbations as large as 10% (Sine et al., 2008). A previous large scale body wave tomography study finds that the TZ features lateral shear velocity contrasts of up to 14.5% in the upper mantle, one of the largest imaged in the U.S (Schmandt & Humphreys, 2010). The inversion for P wave anomalies, S wave anomalies, and Vp/Vs ratios from the same study reveal significant regions with potential for partial melt to depths of up to 195 km, and possibly to even greater depths.

Surface wave tomography for this same region using both ambient noise and earthquake measurements made across the TA has also found anomalously low shear velocity extending from the middle crust to the uppermost mantle (Lin et al., 2009, 2014; Moschetti et al., 2010b). Measurement of Rayleigh wave ellipticity, that is, horizontal to vertical amplitude ratio (H/V ratio; Lin et al., 2014), significantly improved the shallow resolution in the upper crust. The lateral resolution of the imaged structure remains mostly controlled by the average TA station spacing (nominally 70 km) and is unable to resolve smaller scale structures that are directly related to the active geothermal systems. As a result, to better constrain shallower, smaller scale structure in this study area, a dense seismic array and tomographic process capable of finer scale imaging with shallower depth sensitivity is needed.

In this study, we perform ambient noise tomographic imaging of the subsurface beneath the geothermal resource area in South-central Utah, using four temporary dense nodal sub-arrays (Trow et al., 2018): FORGE, Dog Valley, Crater Knoll, and Twin Peaks (Figure 1). The increasing availability of large-N autonomous nodal geophone systems has made high resolution shallow imaging based on ambient noise possible (e.g., Lin et al., 2013). For this study, we follow previous ambient noise tomography studies, such as Bensen et al. (2007) and Lin et al. (2008), for our seismic processing methodology. We combine data: (a) from arrays deployed at different times, noting that the seismic noise field of each deployment has significant potential to vary, as the deployments span all four continental seasons, and, (b) that include regional, permanent broadband seismometers and thus multiple different datasets of different types have been integrated. This project confirms the feasibility of combining data from asynchronous seismic deployments and a permanent regional network using noise cross-correlation and array analyses to generate informative shear velocity models of the subsurface (Jia & Clayton, 2021).

2. Data

The data set consists of continuously recorded seismic data from four separate, temporary, geophone deployments (Trow et al., 2018). Each deployment lasted approximately 30 days and collected data at different times of the calendar year (Figure 1). The Dog Valley, Twin Peaks, and Frontier Observatory for Research in Geothermal Energy (FORGE, named after the research facility being constructed in the area) arrays all recorded at 500 Hz sampling rate, whereas the Crater Knoll array recorded at 1,000 Hz. The deployments span more than one year between June 2016 and October 2017. The four geophone arrays are, by design, overlapping geographically to help compensate for the discontinuity in time and to maximize coverage of the area with the dense arrays (Figures 1 and 2). Additionally, we utilize seismic data from permanent, regional, broadband 100 Hz seismometers in the surrounding area that recorded continuously across the entire timeline of all four arrays. Finally, at the inversion stage, we also incorporate phase velocity and ellipticity measurements from the TA broadband stations (Lin et al., 2009, 2014). Some broadband stations were not recording continuously for all of this time, had substantial gaps in the recorded data, or had significant data quality issues, but were still used when they had data

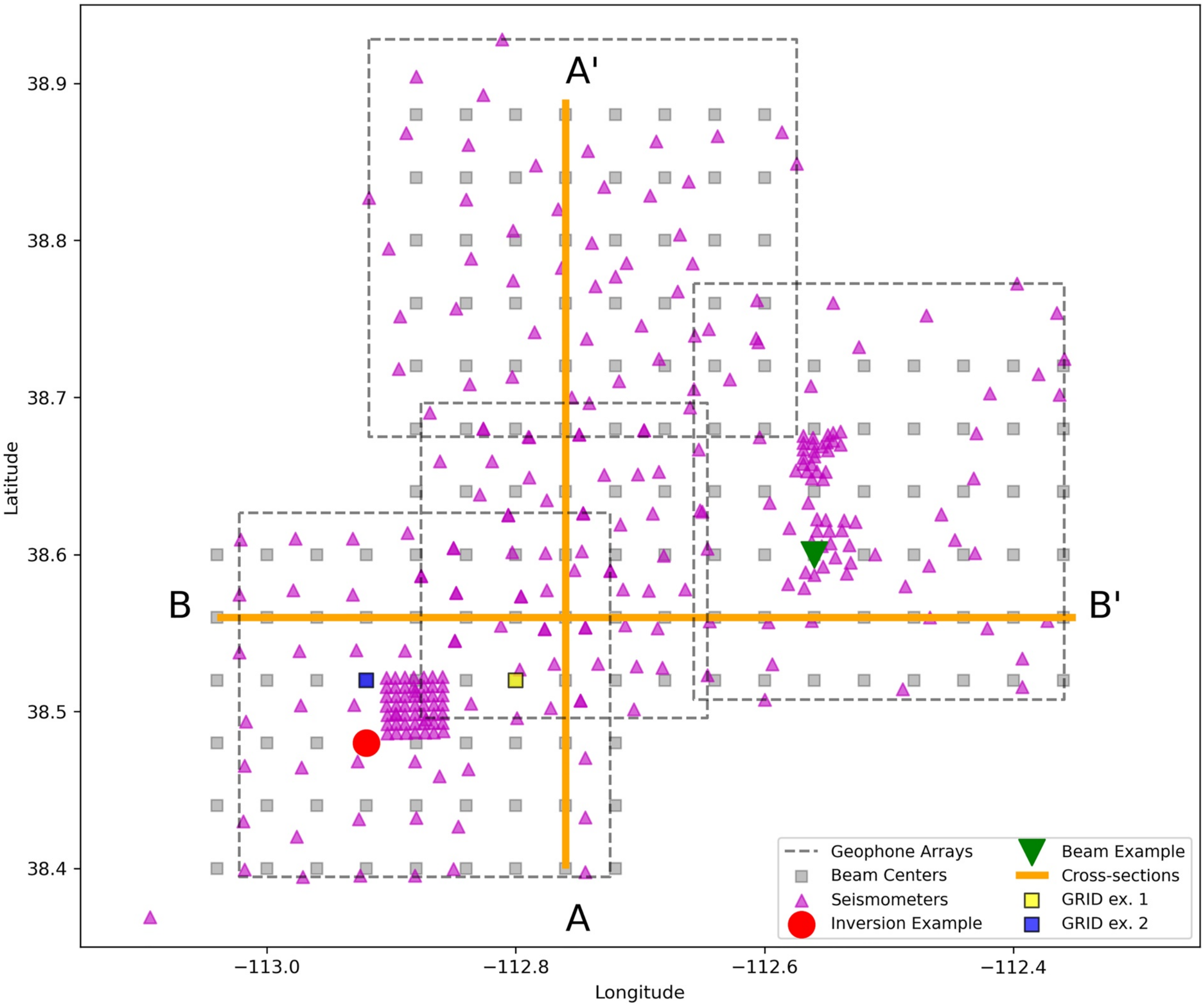

Figure 2. Location of all broadband seismometers and geophones within the study area, every beam center used in the beamforming search, the location of the example beamforming process (Figure 4), the location of GRID ex. 1 and Grid ex. 2 used for ellipticity illustration (Figure 5), the location of the example 1D inversion (Figure 6), and the locations of the cross-sections in Figure 12. The boxes from Figure 1 outlining the sub-array locations have been plotted for reference.

available due to the sparse seismometer distribution in southern Utah. Azimuthal coverage of broadband stations relative to the geophone arrays is substantially more complete to the southwest and northeast than to the northwest and southeast due to permanent station locations that reflect the regional earthquake hazard and historical earthquake distribution, which is concentrated in the Intermountain Seismic Belt, an area that runs approximately north-south on the eastern edge of the Basin and Range province (Smith & Arabasz, 1991).

3. Methods

3.1. Data Preprocessing

We closely follow the preprocessing methodology described in previous ambient noise tomography studies (Bensen et al., 2007; Lin et al., 2008, 2014). Data for all seismometers are cut into daily time series. We remove the mean and trend, and taper at 1% at each end of the time window. We deconvolve the instrument response for all data prior to additional preprocessing. We again remove the mean and the trend, and bandpass the data between 0.05 and 20 Hz to prevent aliasing before downsampling each time series to a uniform rate of 50 Hz. The data are then cut into 10 min windows. For each 10 min window, we again remove the mean and the trend and again apply a taper of 1%. To retain relative amplitude information between components (Lin et al., 2014), we

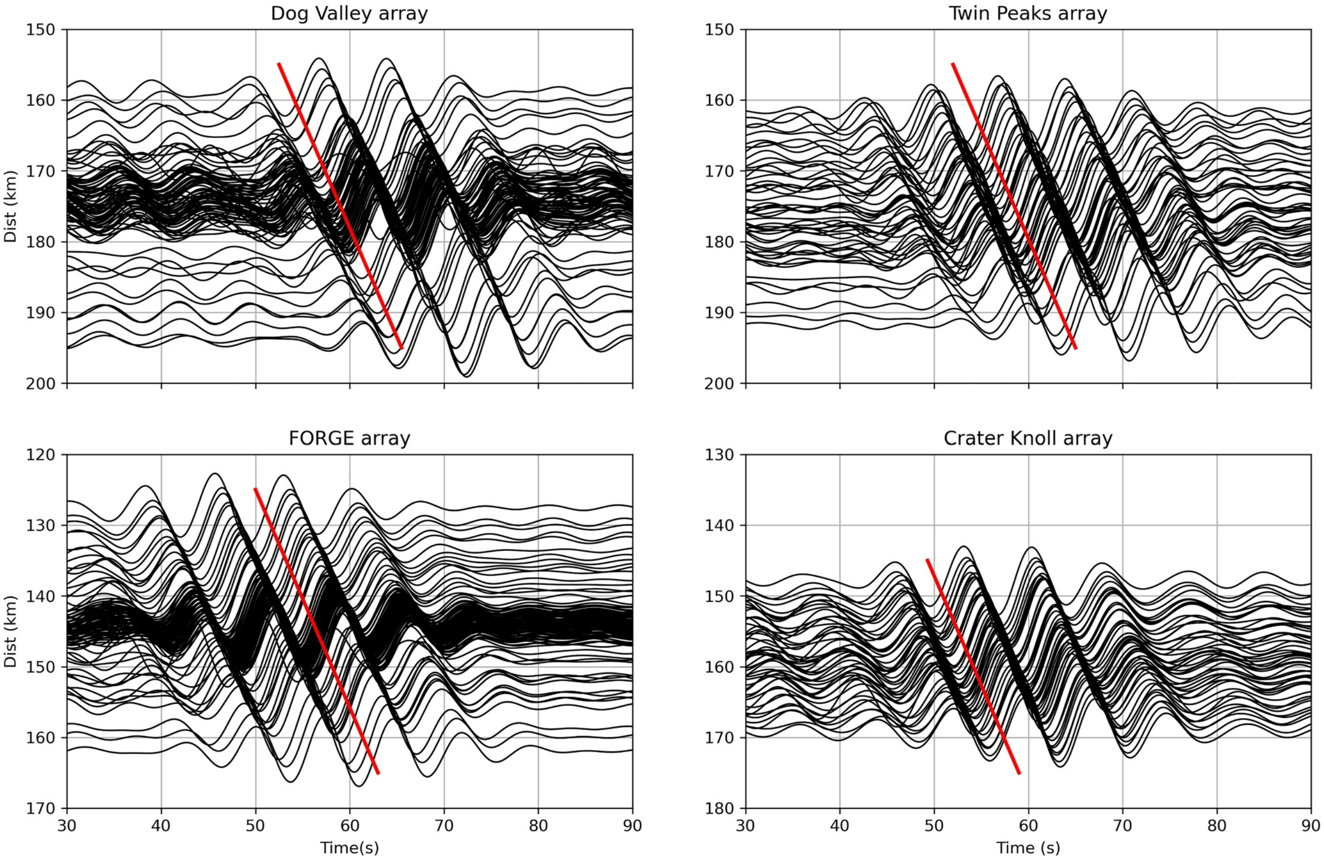

Figure 3. Example ZZ-component Rayleigh wave record-section moveout with broadband station VRUT (Figure 1, inset) as the source and every geophone in each sub-array as the receiver. The correlograms were bandpass filtered with a center period of 7 s. Red lines show 3.1 km/s apparent velocity. The *Y* axis is distance from the virtual source in kilometers. The correlograms are scaled for visibility and have a normalized amplitude of 1.

spectrally whiten each of the windows on all three components relative to the frequency spectrum of the vertical component.

3.2. Cross-Correlation

We cross-correlate data from all stations (geophones and broadband seismometers) with every other contemporaneous station (e.g., Lin et al., 2008, 2009, 2012, 2014; Bensen et al., 2007; Shapiro et al., 2005). Correlations are not performed between geophone deployments due to different deployment dates. To accommodate processing and computer memory limitations, we break this up into two sets: the first set uses all broadband seismometers as virtual sources and virtual receivers, and nodal geophones as virtual receivers only. The second set uses all nodal geophones as both source and receiver. In this manner, we generate correlograms for all station-pair combinations. For each 10 min window of noise, we perform this cross-correlation for each station pair and normalize to the amplitude of the vertical-vertical correlogram, and add this correlated waveform to the previous correlated 10 min windows. In total, the correlograms for each seismometer pair contains the sum of more than 4,000 individual cross-correlations stacked together over an approximately 30-day window, although the exact count varies due to data availability. We perform a full 3 × 3 multi-component cross-correlation, correlating the Vertical (Z), North (N), and East (E) components for a total of 9 correlation combinations: ZZ, ZN, ZE, EE, EN, EZ, NN, NE, and NZ. After correlation, we rotate all components with N and E to radial (R) and transverse (T) components (Lin et al., 2008, 2014), resulting in ZZ, ZR, ZT, RR, RT, RZ, TT, TR, and TZ. The correlograms are also made symmetric by averaging the acausal and causal components. We find that the strongest noise source comes from ocean-wave energy between 5 and 10 s period. Examples of the causal portion of ZZ cross-correlated waveforms record sections with a virtual source station located to the southwest are shown in Figure 3, where clear Rayleigh wave moveouts can be observed.

3.3. Beamforming Tomography

We found empirically that a beamforming approach (Harmon et al., 2008; Roux & Ben-Zion, 2017) was able to produce stable and reliable local Rayleigh wave phase slowness measurements across across the ambient noise cross-correlation wavefields (Lin et al., 2013). To do this, we first apply a two-pass, four-corner bandpass filter on correlograms by using six distinct periods: 5, 6, 7, 8, 9 and 10 s, with corner frequencies that are plus/minus 20% of the target period. For each period and each virtual source (broadband stations, Figure 1), we construct the cross-correlation wavefield across the study area using all ZZ noise cross-correlograms between the common source station and all geophone stations. We then apply beamforming across the wavefield to determine both the location-dependent phase velocity and direction of propagation.

To create the beam centers, we arrange a grid to cover the entire combined geographic area beneath each geophone array. These beam centers were uniformly distributed with a spacing of 0.04° (approximately 4 km) for both longitude and latitude (Figure 2). Spacing was performed in degrees for convenience. We use an empirically selected beam width of 12 km to maximize our structural resolution capabilities without creating excessive error due to low correlogram count per beam, and we maintain this beam width across all period ranges to create consistent lateral resolution. We perform the beamforming procedure for all six distinct periods.

To perform beamforming for a given virtual source, we apply time corrections to all correlograms with receivers within the beam based on the presumed wavefield azimuth and phase velocity and stack the resulting shifted correlograms (i.e., slant-stack). For each geophone, the time correction is calculated by first projecting the distance between the geophone and the beam center d onto an assumed azimuth φ of travel of a plane wave. This calculation is as follows:

$$d' = \cos(\phi - \varphi)\, d \tag{1}$$

where d' is the projected distance and ϕ is the azimuth from the beam center to the geophone. For an assumed phase slowness s (inverse of phase velocity), the time correction Δt is then calculated as:

$$\Delta t = sd' \tag{2}$$

We take the envelope function of the stack correlogram and take the maximum envelope amplitude as the beam power. We perform a two-step 2D grid search of slowness and azimuth between 0.15 and 0.7 s/km and 0°–360°, respectively. A coarser increment of 0.02 s/km and 20° are used in the first step where a finer increments of 0.002 s/km and 2° are used in the second step to search the area surrounding the maximum beam power from the first step. The preferred slowness and azimuth is determined based on the maximum beam power from the second step (Figure 4).

While this searching procedure is only performed on the ZZ component correlograms, we also stack the ZR, RR, and RZ components, using the preferred slowness/azimuth from the search on the ZZ component. With a stack of all four of these components for each beam, we take H/V measurements at each discrete beam center instead of at each physical geophone location, which is described in Section 3.4.

For each beam center, this entire procedure is repeated for every virtual source (permanent stations, Figure 1), and all slowness and H/V measurements for each beam center are used as the collection of measurements for that beam center. Depending on available correlograms, this process results in 20–30 slowness measurements for each beam center and each period. After slowness measurements are taken, measurements from stacked waveforms with a computed signal to noise ratio (SNR) of less than 5 are discarded, retaining 95% of the original measurements. Then, we apply an iterative process to discard measurements more than 3 standard deviations away from the mean is applied as described in Berg et al. (2018), resulting in 16,258 total measurements across all periods, or 89% of the original measurements. The remaining measurements are averaged. We use standard deviation of the mean for uncertainty at each beam center for phase velocity. However, we imposed a minimum input data uncertainty of 0.05 km/s for grid locations below an empirically chosen measurement count of 10 to account for higher uncertainties with very few measurements that may, by chance, agree well with each other.

In this study, SNR is measured in accordance with the definition of Bensen et al. (2007), which uses the maximum amplitude of a signal window based on expected arrival and the root-mean-square amplitude of a later noise window (Figure 4d). However, we adjust the method to match our correlogram data set as follows: we define

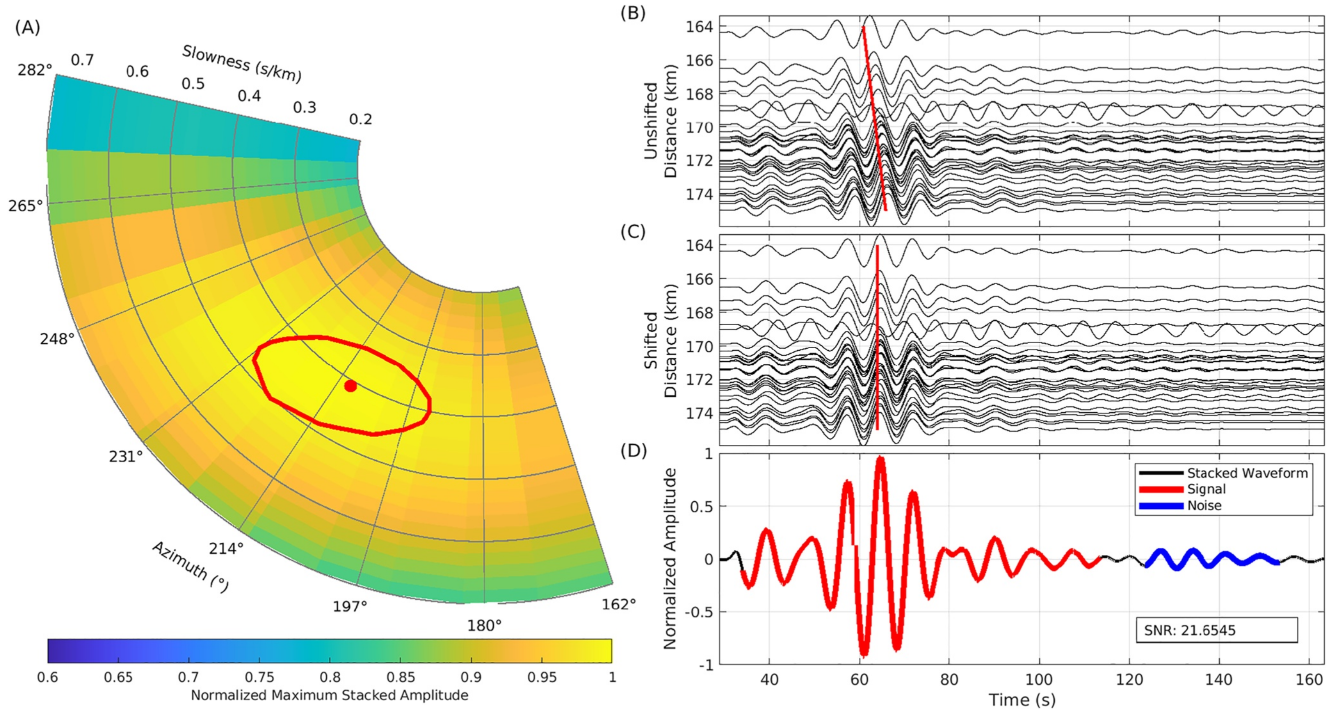

Figure 4. Example beamforming process for one beam center with seismometer VRUT (Figure 1) as the source. This particular beam is in the densest part of the Dog Valley sub-array, resulting in the inclusion of many individual correlograms. Location is shown as a green triangle in Figure 2. (a) Polar plot showing stacked beam amplitude as a function of azimuth and slowness. The maximum amplitude slowness and azimuth is shown as a red dot. 95% of the maximum is contoured in red. (b) Original, un-shifted waveforms. (c) Shifted waveforms corresponding with the maximum stacked amplitude. (d) Stacked waveforms from panel (c), showing the signal and noise windows for SNR calculation. Panels (b–d) share the same time axis.

the signal window based on the maximum and minimum theoretical velocity of 5 km/s and about 1.42 km/s, corresponding to the slownesses used in the grid search. As a result, our signal window varies inherently as a function of distance from the virtual source. In addition, we use a fixed 10 s window between signal and noise, and a fixed 30 s noise window following this gap. The reason for this simplified, one-size-fits-all approach is due to the natural tendency of stacking waveforms to reduce random noise in the stacking process, making more complicated SNR criteria unnecessary.

3.4. Ellipticity (H/V) Measurements Through Beamforming

We follow the concepts described in Lin et al. (2014) and Berg et al. (2018), to extract ellipticity, or H/V, measurements to better constrain shallow structure. The ellipticity measurements of Rayleigh waves have depth-sensitivity that is far shallower than phase velocity (Tanimoto & Rivera, 2008). We employ the beamforming approach as described in the previous Section 3.3 for signal enhancement and to ensure that our lateral resolution is identical to that of the beamforming tomography. This replaces each individual receiver with the stacked waveforms at each beam center—the broadband seismometers serving as virtual sources remain the same.

As in the slowness measurements, all correlograms were made symmetric by averaging the causal and acausal components. We compute the envelope function of the four stacked cross-correlation components. We follow the methods of Lin et al. (2014) to measure Rayleigh wave H/V ratios of these stacked correlograms, which averages vertical and radial excitation for a given station as a source and as a receiver. However, since we are only concerned with the H/V ratios within our study area, we focus only on receiver ellipticity measurements—namely, ZR/ZZ and RR/RZ, with broadband seismometers as source stations. We discard any measurements involving a correlogram with an SNR of less than five. For example, if ZR has an SNR of less than five, but ZZ has an SNR of greater than five, ZR/ZZ would not be used. If only one measurement (ZR/ZZ or RR/RZ) passes this criterion, that measurement is used alone. If both measurements (ZR/ZZ and RR/RZ) pass this criterion, we average the two receiver measurements. Non-ZZ correlograms generally have a much lower SNR, so imposing

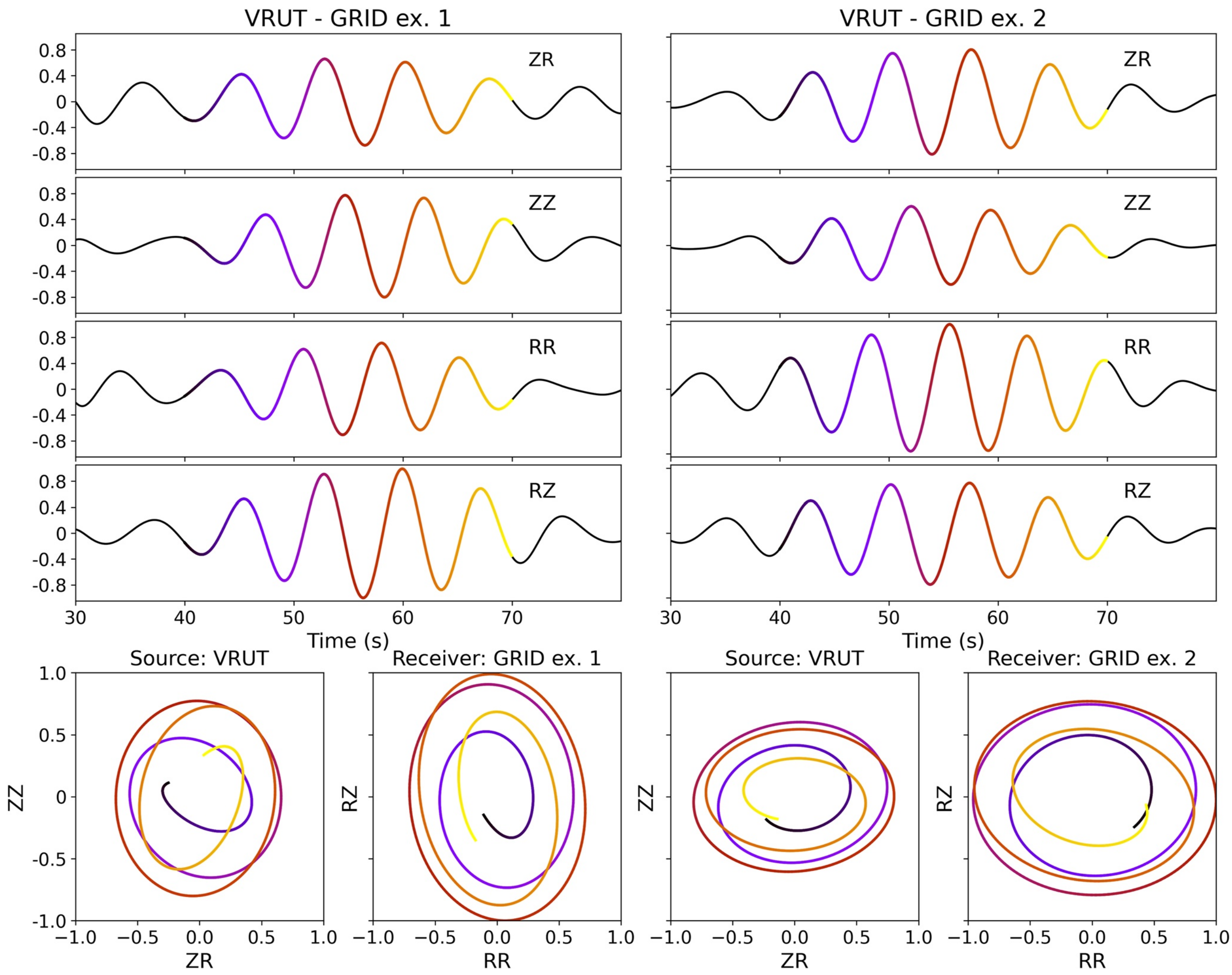

Figure 5. Example particle motion using broadband seismometer VRUT (Figure 1) as the source seismometer and two example beam centers from the FORGE sub-array. Locations are shown in Figure 2. (a) GRID ex. 1: a grid point/beam center that is located on the flank of the Mineral Mountains (Figure 1) and has particle motion elongation in the vertical direction. (b) Grid ex. 2: A grid point/beam center that is located in a basin and has ellipticity that is elongated horizontally. All components are labeled by their respective correlogram. The signal was bandpassed centered around 7 s period. Clear retrograde Rayleigh wave particle motion is observed on all four components. Correlogram amplitudes are normalized relative to the maximum amplitude component.

the same SNR criteria of five at minimum results in retention of only 22% of the original measurements. We apply an identical, iterative process to discard outliers as described in Berg et al. (2018) and in the previous section, resulting in retention of 5,807 measurements across all periods, or 21% of the original measurements.

An example of particle motion for the stacked correlograms illustrating the ellipticity for two discrete beam centers is shown in Figure 5. The result of repeating this beamforming process is up to 30 independent ellipticity measurements for each beam center and each period—one for each broadband seismometer virtual source. To obtain the final H/V ratio for each location, we average all measurements. To compute uncertainty, as in the beamforming tomography, we use the standard deviation of the mean of H/V measurements for each beam center.

3.5. Joint Ellipticity and Shear Velocity MCMC Inversion

We used a Monte Carlo Markov Chain (MCMC) Bayesian non-linear inversion technique to jointly invert phase velocity measurements and ellipticity measurements for a 1D shear velocity profile at each beam center grid point. This inversion process has been widely documented and tends toward fully sampling the posterior distribution of the model space with sufficient run-time, reduces the chances of failing to find the global minimum residual solution, and allows for quantification of uncertainty (Berg et al., 2018; Mosegaard & Tarantola, 1995; Shen et al., 2012). The method employs a "random-walk" method to sample most of the model space, and also incorporates random "jumps" within the model space to ensure sufficient exploration. The discretization of Rayleigh wave phase velocity measurements and ellipticity measurements onto the same 2D grid was a deliberate decision to facilitate consistent resolution on the joint inversion for shear velocity. In addition to the new data presented in this paper, we included regional lower resolution TA phase velocity measurements (Lin et al., 2009), at 12, 14, 16, 18, and 20 s, and ellipticity measurements (Lin et al., 2014) at 10 and 12 s. This was a deliberate decision to stabilize the models at depth, and force a smooth transition to existing regional scale, deeper models. Additionally, to account for resolution discrepancy between the two datasets, the uncertainty of the TA phase velocity data was scaled up to match the average uncertainty in the beamforming phase velocity measurements, with TA H/V measurement scaled to be approximately the same percentage relative to HV uncertainty measurements from the 2D single beamforming. To avoid conflicting excessively with adjacent period beamforming measurements, the uncertainties of the lowest period TA data for both phase velocity (12 s) and ellipticity (10 s) were scaled up an additional 20%.

We chose B-splines as basis functions for two reasons. The first is that surface waves are generally insensitive to sharp seismic impedance boundaries, so a smooth model—inherent with B-splines—was a natural choice. The second reason is that B-splines allow for minimal parameterization in the inversion, with only one parameter per B-spline. We tested various B-spline versus depth distributions to determine the most appropriate distribution for the data, which was characterized by decreasing spline density with increasing depth (Lin et al., 2013).

The initial model was based on a regional, layered, piecewise-constant, continuously increasing 1D velocity model used for earthquake locations (Arabasz et al., 2005). However, the constant velocities of each layer were changed to a gradient and the model was smoothed and interpolated to accommodate the spline-based inversion (Figure 6). We used seven B-splines as the basis for the inversion, distributed over 30 km depth. Based on estimated sensitivity kernels using this regional 1D velocity model (Figure 7), we expect our beamforming data to possess sensitivity between 0 and 15 km depth when including both ellipticity and phase velocity measurements. Depths between 15 and 30 km are controlled primarily by the TA data—here, we focus our interpretation on depths shallower than 15 km.

The inversion parameters were minimally constrained, generally allowing exploration of large ranges of shear velocity values. The most significant limitation we did impose was that the maximum shear velocity cannot exceed 5 km/s, a reasonable value for the crust. We deliberately allowed for non-monotonically increasing shear velocity to account for the possibility of LVZs, which we expected as a strong possibility given the regional geology and previous seismic imaging studies. The MCMC process was run for 3,000 "random-walk" iterations over 8 random parameter initializations, or 'jumps' in the model space for each 1D inversion. The final suite of models only includes those that have a misfit that is within 20% of the minimum misfit model. When computing misfit, we weight the phase velocity residuals in the misfit of the inversion more strongly by a factor of two. That is, the misfit is determined 2/3 by phase velocity residuals and 1/3 by H/V residuals.

When quantifying uncertainty of the model, we use the standard deviation of the range of posterior models for each grid point. We use this as a substitute for error propagation through the inversion process by allowing full model space exploration and only requiring the data and its uncertainty to calculate probability of model acceptance. In practice, this results in some depths and locations with uncertainties as high as 10% (Figures 11c and 11d), which can be attributed to lower SNR, and associated higher uncertainty, in some periods for both ellipticity and phase velocity measurements.

4. Results

4.1. Stacked Correlograms

The resulting correlograms capture ambient noise dominantly coming from the southwest in the oceanic secondary microseism period band of 6–8 s (Traer et al., 2012), but signal is observed from 5 to 10 s, although it is not as clear on the edges of this band. An example of this extremely clear energy moveout is in Figure 2, which has been bandpassed centered around 7 s. Although the longer period of oceanic primary microseism around 15 s is not visible, we attribute this to the higher frequency instrument response of the geophones (Lin et al., 2013; Trow et al., 2018; Wang et al., 2019). Based on the apparent moveout velocity and the particle motion of these

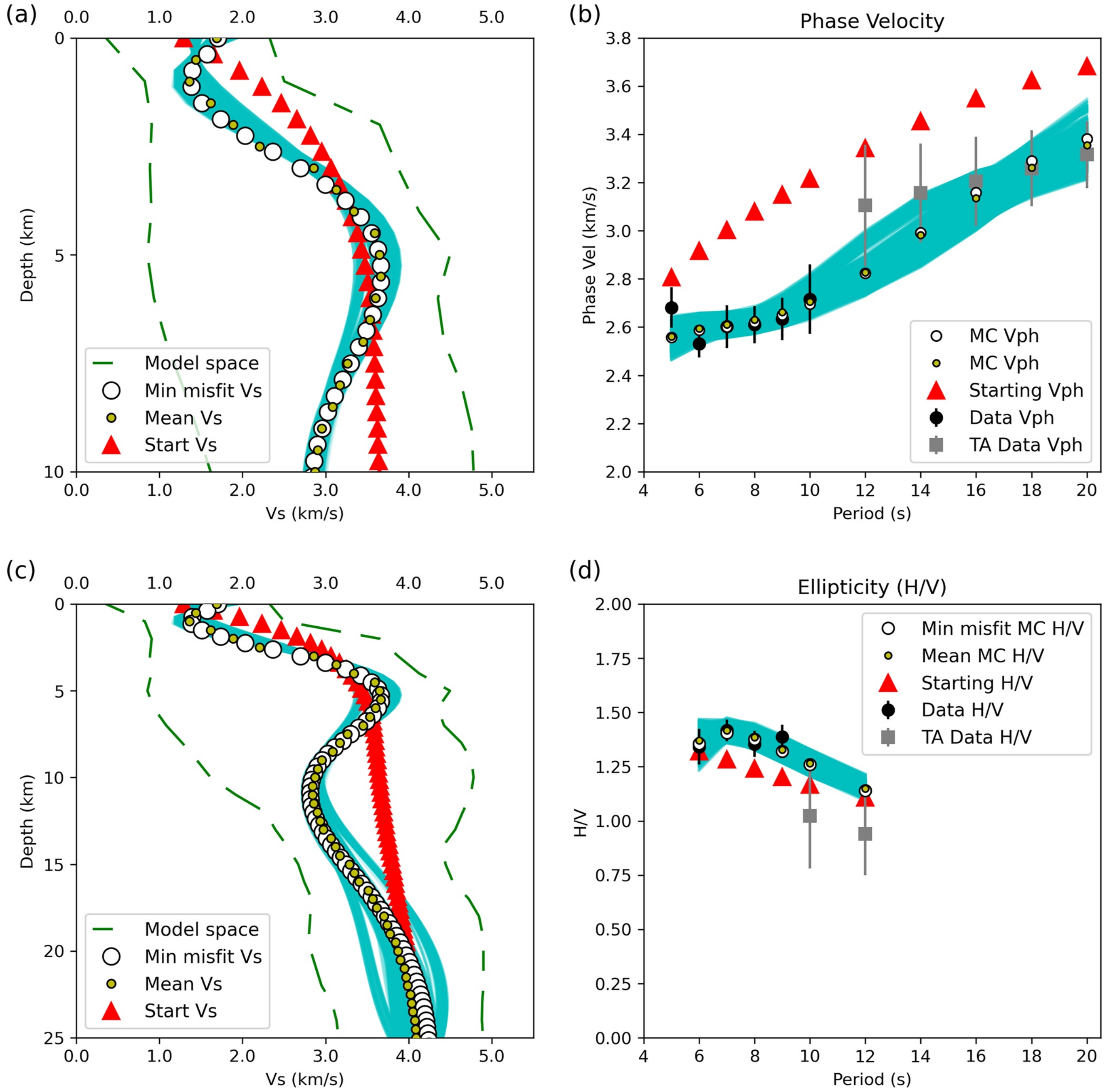

Figure 6. An example 1 D velocity model near the dense FORGE array. Location of this model is shown as a red circle in Figure 2. (a) 1D Shear velocity model, 0–10 km depth. White circles are the minimum misfit model. Red triangles are the starting model. Yellow dots are the average model of all models shown. Turquoise lines are all posterior models. Green dashed lines represent the bounds of all explored models. (b) Comparison between model predicted and observed phase velocities. Measurements made in this study and previous TA measurements are shown with different symbols. (c) Same as (a), but to 25 km depth. (d) Same as (b), but for H/V (ellipticity).

waveforms (Figures 3 and 5), it is clear that the dominant signal we recover with these deployments comes from Rayleigh waves. We note that clear moveout is observed between the broadband seismometers and the geophones, even with station pair distances exceeding hundreds of kilometers. These long range correlograms comprise the entire data set we used in this study as short distance 5–10 s geophone to geophone correlograms are indistinguishable from autocorrelations and unsuitable for velocity measurements. Note that we do not have intermediate distance inter-array geophone correlograms due the temporal gap in deployment.

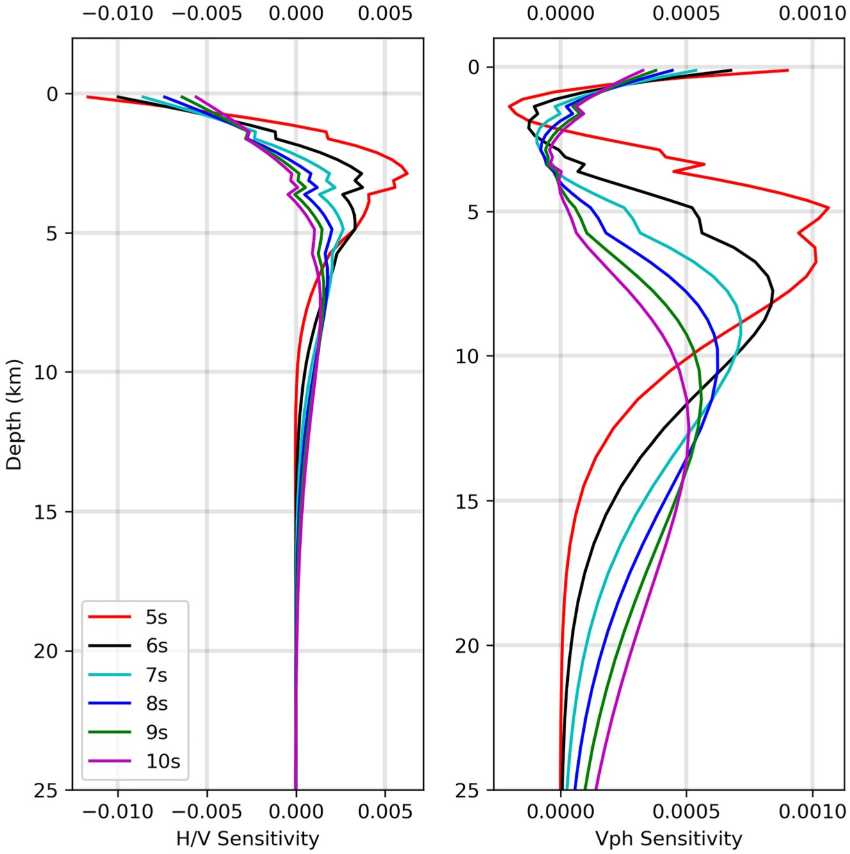

Figure 7. Estimated sensitivity kernels for periods of 5–10 s computed using the regional, 1D velocity model (Arabasz et al., 2005). Left: H/V sensitivity kernels. Right: Phase velocity sensitivity kernels. "Kinks" in the sensitivity arise from sharp contrast between laterally homogeneous layers.

Whereas previous dense nodal arrays deployed in other regions have had success in extracting shorter period surface waves for shallow imaging (e.g., Lin et al., 2013), little to no moveout is observed at periods shorter than 4 s. The only other period range with visible moveout is in the densest part of the FORGE and Dog Valley arrays, where we observe noisy moveout between 1 and 4 Hz (0.25–1 s) when nearby nodal geophones are used as the source stations. Because this signal is not ubiquitous across our study region, we ignore it for the purposes of this project. Future work will likely involve studying this signal on the densest part of the arrays to image much more localized structure near the surface.

4.2. Beamforming Tomography

We find that by using the beamforming with both an azimuthal and slowness search, we are able to recover realistic and consistent phase velocity measurements across our study area between 5 and 10 s period (Figure 8). We note that the observed velocity structure appears to be coherent across the four asynchronous nodal geophone deployments, demonstrating that stitching together spatially overlapped nodal arrays with potentially different, seasonal ambient noise seismic wavefields is not only possible but feasible. We note that there is also good continuity of phase velocity features between each period. The low and high velocity zones generally change smoothly with changing periods, allowing a continuous tracking of the observed anomalies. Additionally, we note that the anomalously slow phase velocity regions coincide with the regions of increased measured surface heat flux (Figure 8), further corroborating our velocity structure findings. The low phase-velocity areas additionally coincide with known surface manifestation of subsurface heat, namely hydrothermal systems currently visible in the form of hot springs and/or in their usage in geothermal energy.

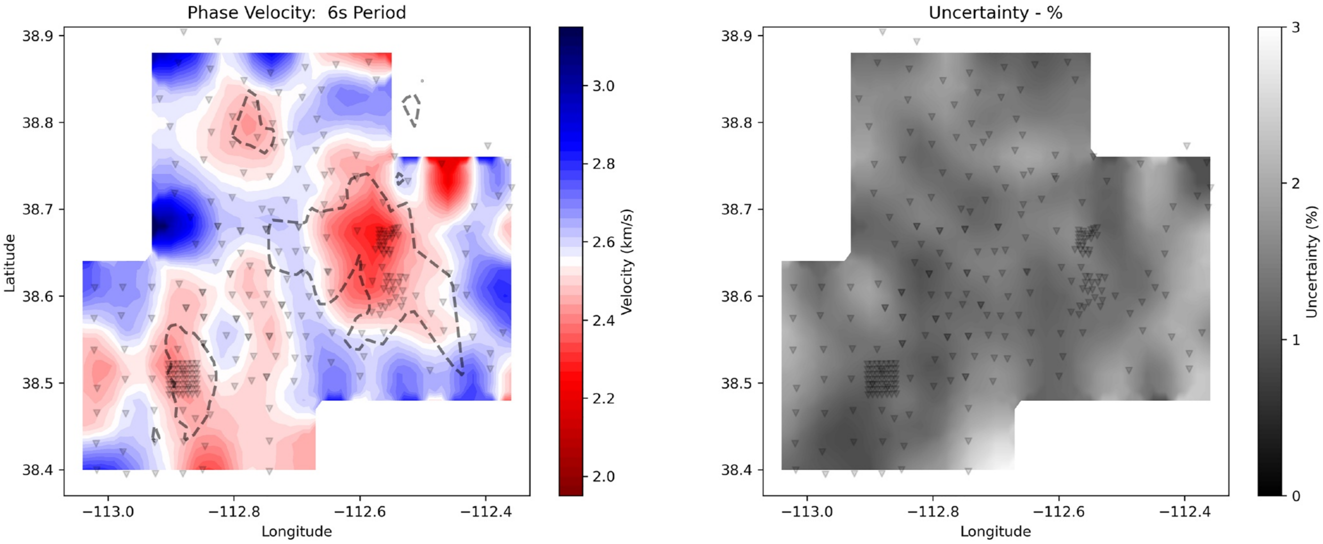

Figure 8. (Left): The 6 s phase velocity map derived from performing the beamforming process for all beam centers illustrated in Figure 2. Dashed lines are surface heat flux contours (Figure 1). (Right): Uncertainty of 6 s phase velocity measurements, measured by standard deviation of the mean, and expressed as percentage of the mean value. The slow velocity anomalies are consistent with the areas of high surface heat flux (red lines, Figure 1). In general, the errors, computed based on standard deviation of the mean, are far smaller than the observed velocity variations in the study area. Gaussian interpolation has been applied for visualization purposes only.

4.3. Ellipticity Measurements

In general, we find clear Rayleigh-wave-like retrograde particle motion between 5 and 10 s, with the most consistent and best measurements between 6 and 8 s (Figure 5). However, due to overall lower SNR in non-ZZ components at 5 and 10 s period, we do not use ellipticity measurements at these two periods in the inversion process. Similar to previous ambient noise tomography studies (e.g., Berg et al., 2018), we see higher (>1) H/V ratios in basins and lower (<1) ratios in mountainous areas where we expect competent rock to be found closer to the surface (Figure 9). We note that estimated sensitivity kernels of H/V ratios (Lin et al., 2014) in the period range of 5–10 s using the regional 1D reference velocity model (Arabasz et al., 2005) place the depth sensitivity of our ellipticity measurements between 0 and 5 km below the surface (Figure 7). Given this sensitivity, we find

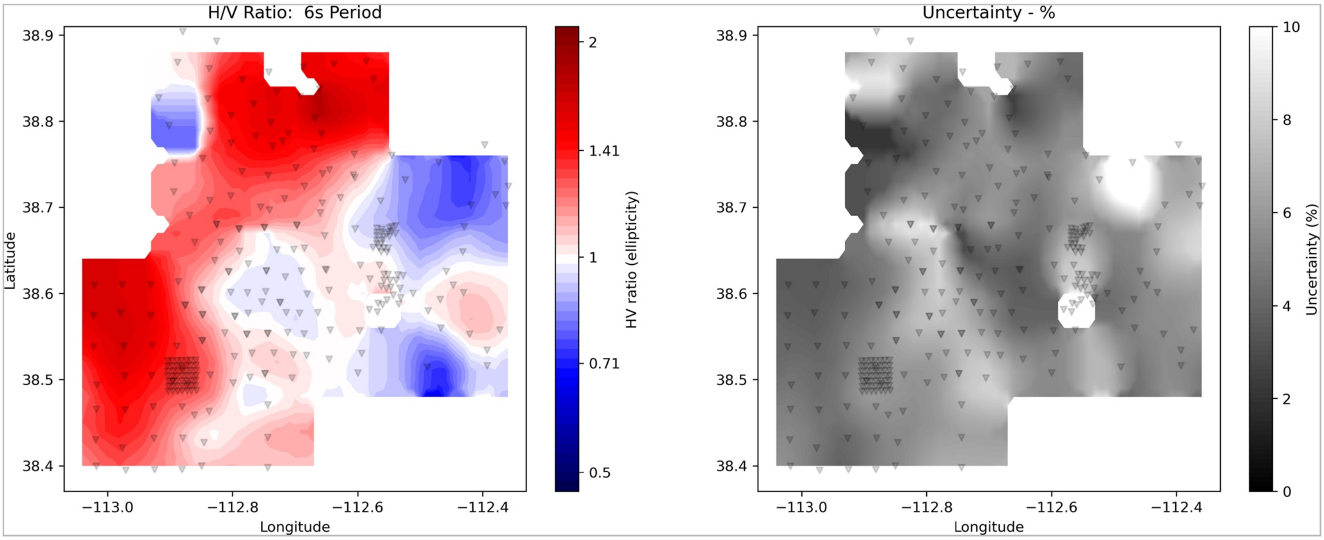

Figure 9. (Left): 6 s H/V measurements across the study area from beamforming. Note that the values within the color bar are spaced logarithmically, since the measurement is inherently a ratio. (Right): Uncertainty of 6 s H/V measurements, measured by standard deviation of the mean, and expressed as percentage of the mean value. We note that the variations in H/V values are far greater than the upper and lower bounds defined by the uncertainties. In general, we find areas of high ellipticity to coincide with known sedimentary basins, consistent with expectations based on previous ellipticity measurement work (Berg et al., 2018; Lin et al., 2012).

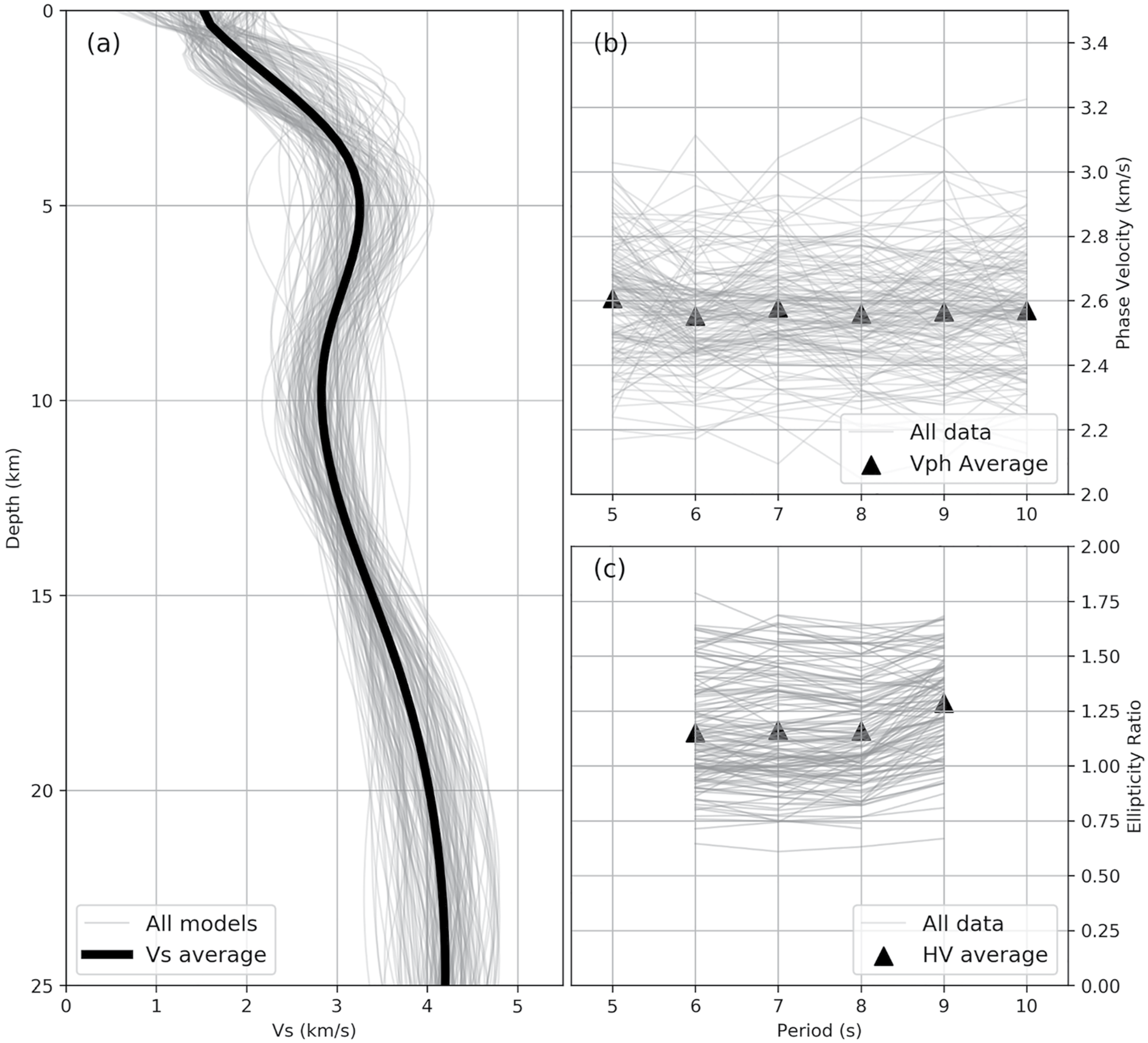

Figure 10. (a) The average shear velocity model of all 155 beam centers (black). Each individual model is plotted in light gray. A clear low velocity zone is visible centered at approximately 10 km depth. (b) Phase velocity dispersion curves of all grid point/beam center measurements. Average measurements are shown as black triangles. Transportable Array data are not shown. (c) The same as (b), but for H/V measurements.

the H/V values consistent with surface geology and basin depth estimations based on gravity data and well logs (Hardwick et al., 2018). We note that while the lowest H/V ratios are as low as 0.5, these values are only found on the edges of our study area and are associated with higher uncertainty. However, H/V ratios less than 1 are found across the study area, especially at periods 6, 7 and 8 s and in the eastern half of the area, indicative of a potential low-velocity zone at depth (Figure 9).

4.4. 1D Monte Carlo Joint Inversion of Phase Velocity and Ellipticity

For most locations, we find that the 1D inversion converges to a stable solution, with almost all of the 155 total inversions featuring a low-velocity zone between 5 and 15 km in depth (Figure 10). This drop represents 13% of the high shear velocity found at 5 km depth: the average velocity drops from 3.25 to 2.82 km/s. This is likely driven by an overall "flat" phase velocity dispersion curve (Figure 10). In addition to plotting dispersion curves for all grid locations, we calculate the slope of the phase velocity versus period for each phase velocity period between 5 and 10 s. We find that the average slope of phase velocity versus period to be slightly negative

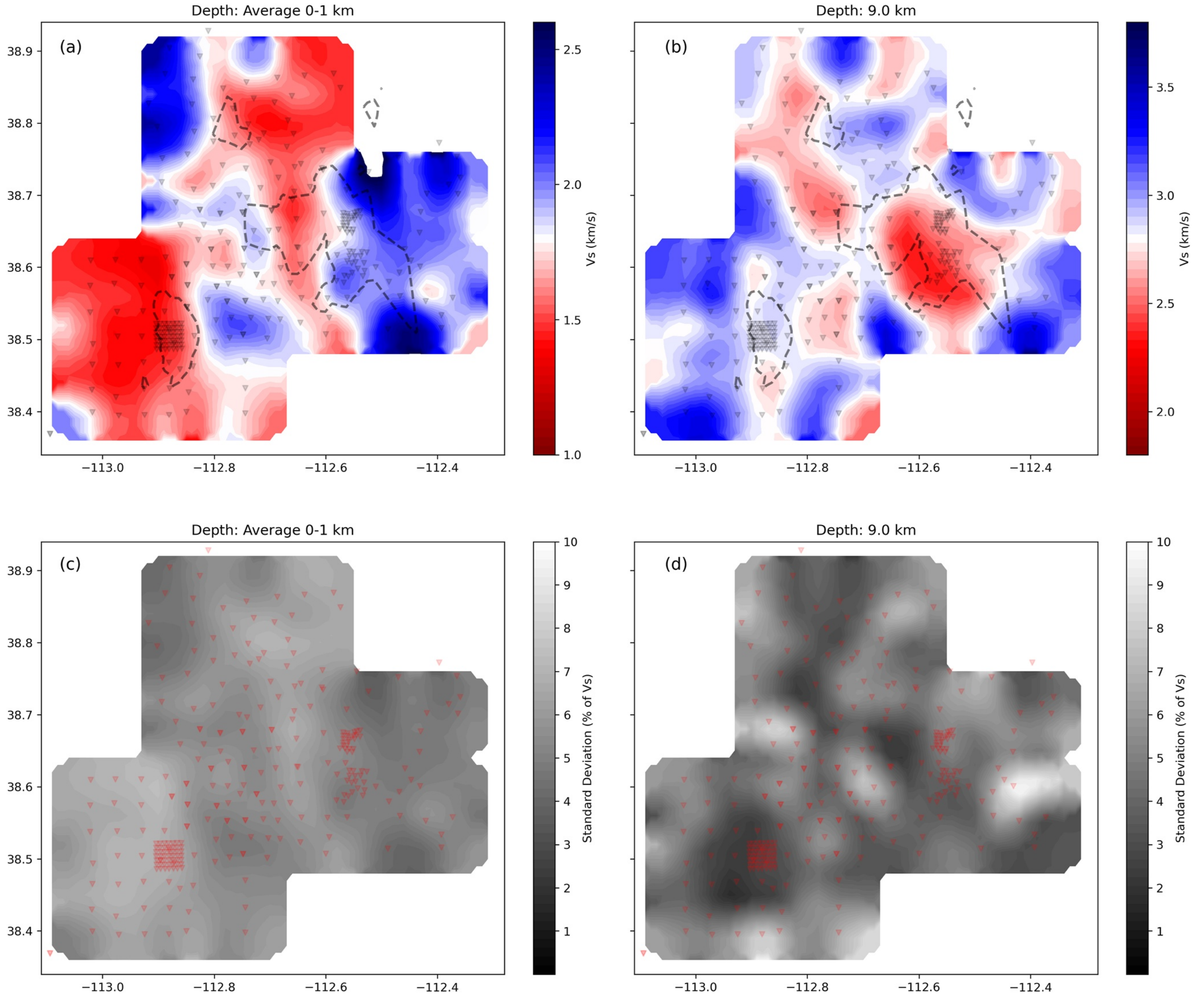

Figure 11. Gaussian-smoothed shear velocity slices at discrete depths. The locations of the geophones have been shown lightly as red triangles in the foreground for reference. For panels (a, b), the surface heat flux contours from Figure 1 are plotted as dashed lines. (a) Depth slice of velocity averaged from 0 to 1 km depth. (b) Depth slice of velocity, 9.0 km depth. (c) Depth slice of uncertainty, averaged from 0 to 1 km depth. (c) Depth slice of uncertainty, 9.0 km depth. The overall velocity patterns in (a, b) are consistent with the patterns of H/V and phase velocity maps shown in Figures 9 and 8, respectively, which is expected based on the depth sensitivity kernel analysis.

(Figure 10b)—indicating that, on average, phase velocity decreases slightly with increasing period. This is a further indication of a LVZ.

The posterior distribution of each 1D inversion is usually fairly narrow in the top 10 km where we would expect to have sensitivity, and generally grows wider with depth below 15 km, as would be expected given the low resolution and scaled uncertainties of the incorporated TA data. In some models, we observe a bimodal distribution between 10 and 20 km depth. This could stem from poor constraint of phase velocity at 9 and 10 s and scaled higher uncertainty in the TA phase velocity data at 12 s (Figure 6), as this is the range that transitions from being controlled by the beamforming measurements to the TA data. The low velocity feature found near 10 km depth is consistent throughout most of the study area (Figure 10). In addition, there are few outliers—the individual models themselves tend to cluster fairly closely around the average model.

We do find that, in some locations, there is a sharp contrast in velocities in between the shallowest 1–2 and 2 km or deeper, driven by some anomalous H/V ratios at shorter periods and/or at the edge of the geophone arrays

(Figure 10). This anomaly was even stronger if we chose to include the less reliable 5 and 10 s H/V data in the inversion. Calculated sensitivity kernels of H/V ratios between 6 and 9 s indicate this may be due to a resolution limitation, resulting in poorer constraint on the shallowest two model parameters, as there can be some trade-off between them due to spline spacing. As a result, we refrain from over-interpretation of the fine scale depth variation of the shallow portion of the model. Instead, we only present the depth average model in the top 1 km (Figure 11a), which is still considered quite robust.

4.5. 3-D Shear Velocity

When each 1-D shear velocity model is combined, a pseudo-3D shear velocity model is created. Because there can be some large contrasts between adjacent models, we apply a Gaussian smoother across each discrete depth (Figure 11). The Gaussian smoother is parameterized to use the 3 closest grid point measurements for interpolation onto a 0.01° longitude (0.88 km) by 0.01° latitude (1.08 km) degree grid, with a maximum Gaussian half-width of 0.05° (maximum of 5.5 km). The exact Gaussian half-width is determined by the maximum distance to the 3 closest grid points. The spacing between measured grid points is 0.04° (about 3.5 and 4.4 km for longitude and latitude, respectively). In general, the model is fairly well-constrained between 0 and 15 km depth. This depth range corresponds to the depth sensitivity range for the data range used (5–10 s), with ellipticity constraining the shallow portion (0–5 km) and phase velocity constraining the deeper region of the model. Below 15 km, the TA data is primarily determining the model values.

Depth-sensitivity kernels (Figure 7) illustrate that ellipticity is the primary factor controlling the velocity in the top 3 km (Figure 11a). However, we note that due to physical access limitations on geophone placement, some surface topographical features are not as visible as we expected, such as the Mineral Mountains (Figure 1), where higher H/V ratios would be expected. As a result, mountainous regions are geographically undersampled by geophone placements compared to the basin regions.

We find that a LVZ between 5 and 15 km depth is a prominent feature in most of the study area (Figure 10a). However, not all areas see an equal low velocity drop. There are several different locations (Figure 11b) correlated with higher heat flux that feature a much lower calculated shear velocity than the surrounding area, most notably the large LVZ in the eastern half of the study area beneath the Crater Knoll and Dog Valley arrays (Figure 1). Figure 12, showing two discrete cross-sections bisecting the study area, highlights the lateral continuity of the low velocity structure and consistency regarding average depth. This pattern is similar to that imaged in the Coso geothermal area in California (Yang et al., 2011).

4.6. Synthetic Dispersion Curves

To test the sensitivity of the phase velocity and ellipticity measurements of the imaged LVZ, we compute synthetic dispersion curves based on the average velocity model across the study region (Figure 10a). We compare this with synthetic dispersion curves from the same velocity model, but with the LVZ removed (Figure 13). We find a significant improvement in fit to the observed average data by including the LVZ compared to not, as measured by least squares misfit. Perhaps more importantly, the model with the LVZ predicts a flatter phase velocity dispersion curve that is more consistent with the observation. The largest improvement in fit is in phase velocity, as might be expected given that the regional velocity reversal occurs between 5 and 15 km depth where phase velocity is most sensitive.

5. Discussion

5.1. Methodological Utility

We demonstrate that it is possible to combine asynchronous nodal datasets with broadband data to image the subsurface using beamforming and surface wave phase velocity dispersion measurements, and combine this with H/V ratio measurements for better shallow resolution. The implications of this include the ability to perform tomography and ellipticity studies with older datasets, stitching them together using permanent stations, as well as the ability to enhance tomographic studies by including nodal deployments in a given region of interest from any time period, provided there are broadband stations to use. Jia and Clayton (2021) demonstrated this further

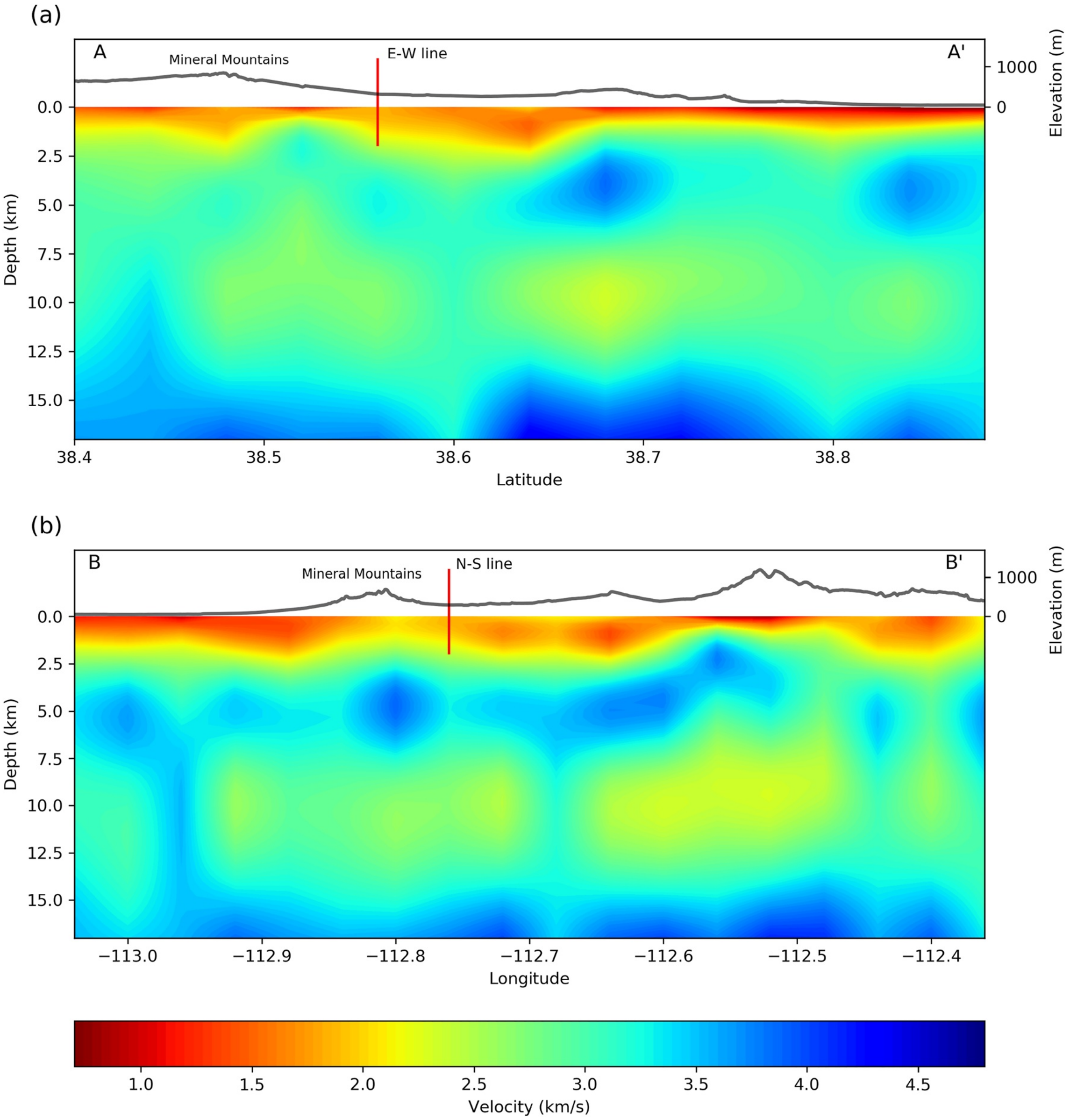

Figure 12. Interpolated shear velocity cross sections across selected vertical profiles. Location of each profile is shown as an orange line in Figure 2. Vertical relief is exaggerated by a factor of two for visualization. The right *y*-axis indicates the elevation of the topography relative to the lowest point in the cross-section, or about 1,500 m above sea level. Depths are plotted relative to the actual surface elevation. No topographic correction has been applied. (a) North-south cross section from A to A'. (b) East-west cross section from B to B′. A significant low-velocity zone is present across most of the study area both latitudinally and longitudinally, but the exact thickness, depth, and velocity varies significantly.

using Frequency-Time analysis (FTAN) and linear, least squares inversion for group velocity, demonstrating that this methodology is robust across at least two separate methods of dispersion measurement.

5.2. The Low Velocity Zone and Its Significance

The cause of the elevated geotherm is uncertain and the location and nature of the source of recent volcanic eruptions are not well known. One key question is whether the geothermally active areas in the study area are connected at depth, and if so, what the lateral extent is. A second question, pertinent to the nature of the heat source, is whether the root cause is primarily from a thin crust and mantle heating associated with the Basin and Range—Colorado Plateau TZ (e.g., Schmandt & Humphreys, 2010), or if it is a region of more shallow

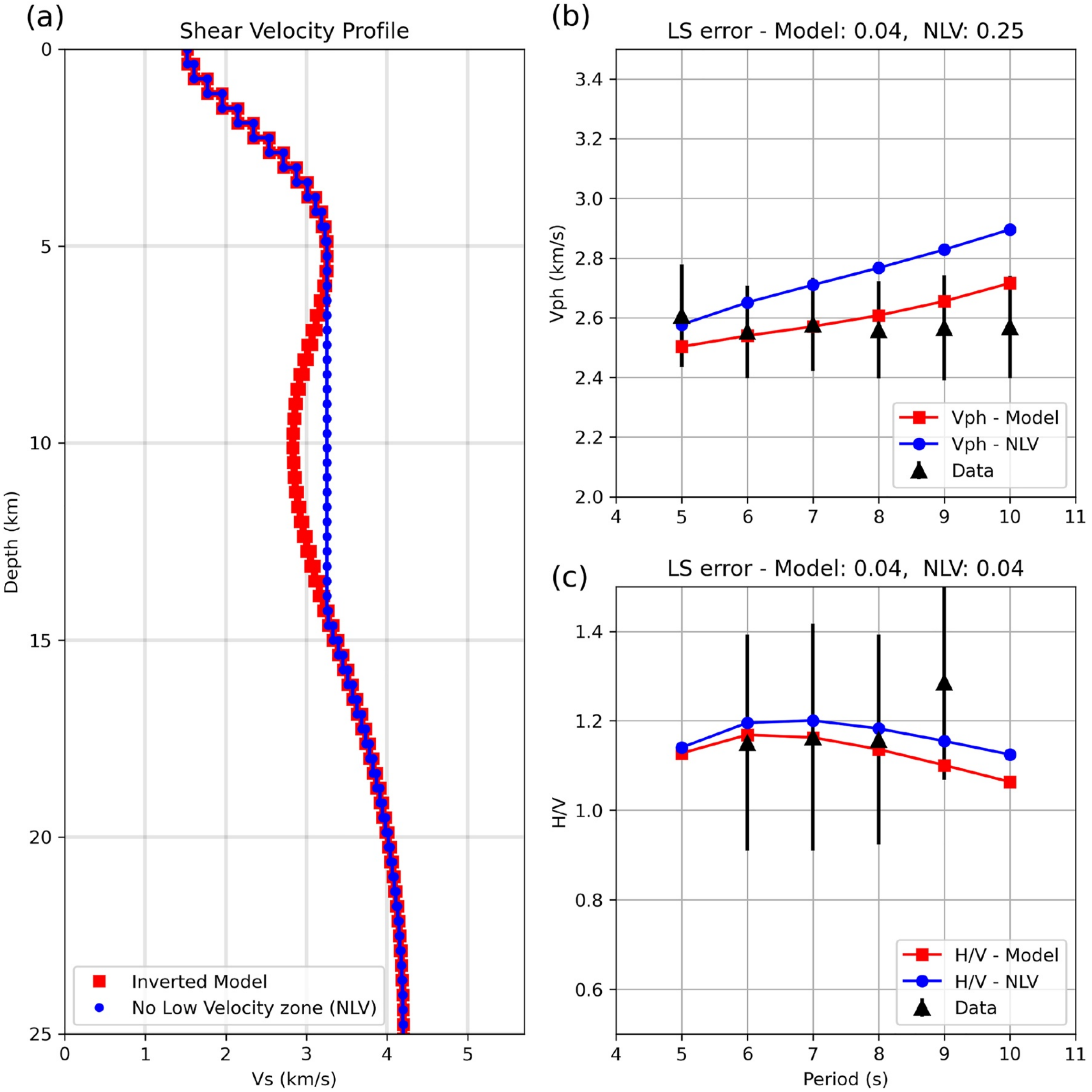

Figure 13. Synthetic dispersion curve test for the average study area model compared to the same model with the low-velocity zone artificially removed. (a) Average shear velocity model, and the average model with the low velocity zone removed. (b) Average model and synthetic phase velocity dispersion curves versus measured dispersion curves, with least-squares misfit printed above for both models. Average phase velocity data is taken across the study area. Standard deviation of all phase velocity measurements across the study area are shown for reference (vertical bars). (c) Same as top right, but for H/V. There is a clear reduction in misfit by including a low velocity zone, primarily for phase velocity data.

magma-sourced fluids, given the Pliocene to Quaternary surface volcanics mapped geologically in the region (Johnsen et al., 2010).

Our work corroborates earlier studies (e.g., Muller & Mueller, 1979; Robinson & Iyer, 1981; Smith et al., 1975; Özalaybey et al., 1997) that detected a zone of low shear velocity at approximately 10 km depth. However, we better resolve the near-surface and lateral structure, and thus find that the anomaly persists across the entire study area with a velocity drop that averages 13% and locally ranges as high as approximately 30%. As no smoothing is applied to either the phase velocity data or the H/V data prior to running each 1D inversion and the smoothing applied after the inversion has a maximum width of 5.5 km, we conclude that features larger than approximately 5 km are robust, as this means the velocity feature is supported by data from multiple grid point phase velocity and H/V measurements.

The largest seismic velocity anomaly occurs in the Dog Valley Region (Figures 1 and 11), in the eastern half of the study area. This anomaly is persistent from depths as shallow as 5 km to depths as deep as 15 km, and coincides with surface geothermal activity (hot springs) and geothermal power plants (Figure 1). This region is also the site of the youngest mapped volcanism in Utah (Johnsen et al., 2010), and recent, shallow earthquakes were recorded suggestive of activity associated with the volcanic structure (Mesimeri, Pankow, Barnhart, Whidden, & Hale, 2021). This Dog Valley anomaly also extends to the southwest with a much lower amplitude toward Crater Knoll and the Mineral Mountains, and spatially coincides with the surface heat flux contours (Figures 1, 8, and 11a).

The local geology suggests elevated temperature and/or interconnected pore fluids as possible causes for the LVZ. If only temperature is considered, a shear velocity decrease from 4 km/s to 3 km/s at 300 MPa confining pressure (10 km depth) requires a temperature increase exceeding 1,200° C (Karato, 1993), and even higher based upon the modeling of Poletto et al. (2018). Additionally, linear extrapolation of well-temperature data (Simmons et al., 2018), sampled at 2,300 m depth from a well drilled within the dense FORGE sub-array, places an absolute temperature of approximately 800°C at 10 km depth. This temperature is insufficient to melt dry granite at a pressure of 300 MPa (Larsen, 1929; Poletto et al., 2018).

However, even a small percentage of water, which is plausible at 10 km depth in a known geothermal area, lowers the onset of melting in rocks by hundreds of degrees (Holland & Powell, 2001). The temperature observations thus permit the presence of hydrous partial melt that may be sufficient to produce the observed velocity anomaly (Poletto et al., 2018). Hammond and Humphreys (2000) examines the effect of partial melt on upper mantle seismic velocities, and finds that even a 1% partial melt can contribute to a seismic shear velocity reduction of approximately 8%. In view of the large magnitude of the velocity anomaly, we suspect that a combination of increased temperature and resulting partial melting is required. However, the effect of such a partial melt on shear wave velocity is difficult to quantify owing to a lack of knowledge of parameters such as porosity, permeability, and the amount of water present at 10 km depth. Previous studies, which assume igneous composition and compositional continuity, offer some guidance for estimating a percentage of partial melt in the middle to upper crust. Chu et al. (2010) would estimate the partial melt percentage of 15%–20% to accommodate such a large drop in shear velocity, while Delph et al. (2021) offers a broader estimation range of between 15% and 28%, assuming igneous rock in the crust. However, real partial melt percentages may differ significantly, as a change in the composition at depth (Allis et al., 2012) and presence of water would substantially lower the shear velocity without the need for such a large melt percentage. Still, we can conclude that a significant partial melt is likely in the LVZ imaged in this study.

Another possibility to consider is large scale radial anisotropy in the Basin and Range Province (Moschetti et al., 2010a, 2010b). Discrepancies between Rayleigh waves and Love waves reveal significant radial anisotropy and is likely responsible for a lower velocity in the middle crust, such as at 12.5 km depth (Moschetti et al., 2010b). Lin and Schmandt (2014) used H/V ratios to examine the azimuthal anisotropy across the western US, which measured a regional average anisotropy of 2%–4% at 10 s period in the region surrounding the Sevier geothermal resource area, which is in agreement with existing tectonic stress models (Heidbach et al., 2010). However, while this anisotropy may play a part in the observed low shear velocity anomaly, it is clearly an insufficient explanation by itself.

Cross-sections (Figure 12) indicate that the source of heat in the Dog Valley area (Figure 1) may be connected at depth to the hydrothermal systems in the FORGE area, both of which feature an operating geothermal power plant. Mesimeri, Pankow, Baker, and Hale (2021) hypothesized that fluid migration along preferential pathways beneath the Mineral Mountains (Figure 1) may have caused recent seismicity. Additionally, the continuity of the LVZ may be explained in part by a silica "cap" formed by silica precipitation by depressurization of rising, geothermally heated fluids forces, resulting in a low permeability layer that confines underlying fluids (Lowell et al., 1993; Saishu et al., 2014). Finally, the two distinct hydrothermal systems may be connected to a single heat source that is too deep to have been imaged in this study.

In contrast to seismic imaging, preliminary results of a recent magnetotelluric survey indicate a large lateral and vertical contrast in resistivity beneath the FORGE array, the Mineral Mountains, and beneath the Crater Knoll array to the east (Wannamaker et al., 2020). A low resistivity body at depths greater than 5 km is located nearly directly beneath the Mineral Mountains and is surrounded to the east and west by higher resistivity. This may indicate that the hydrothermal systems are not directly connected, although they may share a common source of heat from below. This is supported by the fact that, in the FORGE area, test wells drilled into highly continuous impermeable bedrock, below approximately 1 km depth, indicate a low potential for fluid migration (Moore et al., 2020). The observed differences between seismic and magnetotelluric imaging could be related to: (a) the differing material properties to which the methods are sensitive, (b) differences in the geometries of the surveys, (c) differences in the spatial resolution of the methods, and/or (d) the methods used to produce images from the data sets. Given the data used in this study, we expect the vertical velocity contrasts to be well resolved, as surface waves are rather sensitive to vertical impedance contrasts, although the sharpness of such contrasts is not nearly as easily resolvable. In contrast, the inherent lateral resolution determined by the beam widths and beam spacing (12 and ~4 km, respectively) does not allow for sharp lateral velocity contrasts to be resolved in this study. Additionally, the wavelengths represented by the period range used in this study are, at minimum, approximately 10 km, limiting the lateral resolution capabilities regardless of beam spacing. This makes it difficult to laterally resolve any feature smaller in extent than 5 km. As a result of this and the beam spacing, the features discussed here are at least 5 km in lateral extent.

To verify the validity and robustness of the LVZ, we computed synthetic dispersion curves both with and without the LVZ, and significant improvement of fit to the observed data is found with the inclusion of the LVZ (Figure 13). As we noted, the extent of the LVZ seems continuous across the study area. However, the geographic span of geophone instrumentation used in this study may have been insufficient to encompass the full lateral extent of the LVZ, as indicated in Figure 12. Reflectivity studies suggest that this LVZ may also be present in various other areas in the Basin and Range province (Muller & Mueller, 1979; Özalaybey et al., 1997; Smith et al., 1975). It therefore is possible that the LVZ persists across a much larger area than the area covered by the geophone arrays used in this study.

5.3. Comparison to the Coso Geothermal Area in California

The Coso geothermal area is an active and exploited geothermal resource zone in southern California, featuring operating geothermal power plants (Monastero, 2002) and active surface hydrothermal features (Monastero et al., 2005). Coso is very similar to the Sevier geothermal resource area in a number of ways: it features contemporary, active geothermal features and geothermal power plants, a granitic/rhyolitic basement plutonic rock, high surface heat flux, and Quaternary volcanism (Adams et al., 2000; Bacon et al., 1982; Combs, 1980; Duffield et al., 1980; Monastero et al., 2005).

An important distinction, however, is that the Coso system resides in an extremely tectonically active region (Bhattacharyya & Lees, 2002), specifically, the Eastern California Shear Zone (McClusky et al., 2001). In comparison to Coso, there is very little seismic activity in the vicinity of the Sevier geothermal resource area (Arabasz et al., 2007; Kreemer et al., 2012; Mesimeri, Pankow, Baker, & Hale, 2021). However, it nonetheless is useful to compare the Coso and Sevier geothermal areas. In addition to the similarities listed above, Coso features a likely LVZ in the middle/upper crust (Wu & Lees, 1999; Yang et al., 2011). Yang et al. (2011) recovered a shear velocity profile across the area using ambient noise tomography with signals between 3 and 10 s, a similar period range to that used in this study. Their study yielded several different velocity models depending on the strength of the model smoother applied, but in all models except for the most strongly-smoothed, a significant LVZ appears between 5 and 15 km depth with an average depth close to 10 km. This result closely resembles the velocity structure derived from this study. Interestingly, the study area in south-central Utah is geographically smaller than the area covered in the Coso study but the shear velocity perturbation detected appears to be moderately larger on a percentage basis. It is uncertain whether this difference indicates a real difference in subsurface geology or if the two studies differed in their success in resolving velocities in the LVZs.

Finally, it has long been hypothesized that there is an active magma body at a depth as shallow as 8 km beneath the surface at Coso (Bacon et al., 1980). Tomographic studies that imaged an LVZ with anomalously low shear velocity were interpreted to have detected the active magma body (Wu & Lees, 1999; Yang et al., 2011). The geological and geophysical similarity of the Sevier geothermal area to Coso, including the presence of a midcrustal LVZ with shear velocities that perhaps are even more anomalous than Coso, reinforces our suspicion that partial melt is a major contributor to depressed seismic velocities under the Sevier geothermal area. The presence of a hot, partially molten body in the middle to upper crust in Utah not only would explain the high surface heat flow and recent volcanism but it also has important tectonic implications. In spite of scarce shallow seismicity and geomorphic evidence that suggests only minor recent surface deformation (Knudsen et al., 2019), the presence of crustal melt would imply that the Basin-Range to Colorado Plateau TZ remains dynamically active at depth.

6. Conclusion

Using beamforming, ambient noise tomography, and an MCMC inversion, we combine temporally separate nodal geophone datasets with regional broadband data to produce a 3-D shear velocity model of the Sevier geothermal resource area in south-central Utah. We find ocean-generated seismic Rayleigh waves are the most pronounced signal in the area and the most suitable for our target geographic resolution.

We are able to successfully unify different datasets to measure Rayleigh wave phase velocity and ellipticity of a region approximately 70 km square. We observed clear Rayleigh wave move-out between 5 and 10 s on all four geophone arrays. Using beamforming stacking, we demonstrate it is possible to unify the velocity and ellipticity measurements with data from four temporally separate geophone arrays by incorporating continuous broadband data to jointly invert for a 1D velocity structure at each beam center, generating a pseudo-3D shear velocity model of the entire region at a much higher resolution than previously computed. To stabilize the relatively short period inversion of the area, we also utilize the longer period phase velocity and ellipticity measurements previously generated across the Western US documented in Lin et al. (2009, 2014).

The phase velocity and ellipticity measurements from the beamforming algorithm show high correlation with known geologic and geothermal features in the area (Figures 1, 8 and 11). We see a consistency between higher ellipticity with known sedimentary basins in the area, and lower ellipticity with mountainous regions or bedrock close to the surface. Similarly, Rayleigh wave phase velocity measurements have several clear anomalously slow areas which coincide with known locations of high surface heat flux (Figures 1 and 11). These high surface heat flux locations also coincide with existing hydrothermal systems and geothermal power plants in the area.

The final 3-D velocity model from the Bayesian MCMC inversion provides evidence for a rather complex velocity field that is similar to what has been imaged in the Coso geothermal field. Notably, a distinct low-velocity zone is imaged across south-central Utah at depths from 5 to 15 km, corroborating and supplementing the results of previous local seismic imaging work (Muller & Mueller, 1979; Robinson & Iyer, 1981; Smith et al., 1975) and previous regional scale studies (Bailey et al., 2012; Lin et al., 2009, 2014; Moschetti et al., 2010b; Sine et al., 2008). Our explanation for these low velocity anomalies consists of a combination of primarily temperature variation and the presence of partial melt, which is consistent with previous explanations for TZ anomalies (Schmandt & Humphreys, 2010). The 3D model presented in this study helps clarify the extent and shape of the subsurface source of heat responsible for the observed thermal anomalies in the region, and the regional extent and consistency suggest a common heat source for the high heat flow and Quaternary volcanics found throughout the region—which may be a shallower source of magma driven by localized TZ mantle heating. The results we present here provide excellent evidence that more complex geological processes are occurring than Basin and Range radial anisotropy, as the LVZ present in the Sevier geothermal resource area is anomalous even for the Basin and Range. Specifically, TZ-related anomalous heat, originating from the upper mantle, is likely causing some partial melt in the area, causing a seismic LVZ and is likely responsible for the observed surface volcanics, heat flux, and hydrothermal systems.

Data Availability Statement

Heat flow data were provided by Mark Gwynn of the Utah Geological Survey (UGS). Data on Quaternary volcanic deposits and faults are courtesy of the UGS and are publicly available on the Utah Automated Geographic Reference Center (AGRC) database. Figure generation was performed in Matlab and with Python packages *Matplotlib*, *Numpy*, *Pandas*, *Obspy*, *Cartopy* and *Scipy*. Data processing was performed with Seismic Analysis Code (SAC) and the Python package *Obspy.* Seismic data for the FORGE, Dog Valley, Crater Knoll, and Twin Peaks arrays are available on the Incorporated Research Institutions for Seismology (IRIS) database with DOIs Pankow (2016) https://doi.org/10.7914/SN/8J_2016, https://doi.org/10.7914/SN/9D_2017, https://doi.org/10.7914/SN/2F_2016, and https://doi.org/10.7914/SN/1E_2017, respectively. Additional seismic data included broadband stations from the University of Nevada Reno (1971) (DOI: https://doi.org/10.7914/SN/NN), University of Utah (1962) (DOI: https://doi.org/10.7914/SN/UU), and the Leo Brady Network (LB, no DOI available), and were downloaded from IRIS with the python package *Obspy*. Earthscope USArray Transportable Array (DOI: https://doi.org/10.7914/SN/TA) phase velocity measurement data were documented in Lin et al. (2009). IRIS Transportable Array (2003) H/V measurement data were was documented in Lin et al. (2014) and provided by Dr. Fan-Chi Lin.

Acknowledgments
The authors gratefully thank Kevin Mendoza, Andy Trow, Amy Record, Elizabeth Berg, Santiago Rabade, Kostas Gkogkas, and Katherine Whidden for their assistance during the project. The authors also gratefully acknowledge the assistance of Alex Dzubay and Patrick Bradshaw for their comments and suggestions for improvement of the manuscript. The authors thank Cliff Thurber and the associate editor for their review and suggestions to improve the paper. This research was funded by the National Nuclear Security Administration, Defense Nuclear Nonproliferation Research and Development (NNSA DNN R&D). Additionally, part of this work was supported by the National Science Foundation of the United States—Grant EAR-1753362. The authors acknowledge important interdisciplinary collaboration with scientists and engineers from LANL, LLNL, MSTS, PNNL, and SNL. Sandia National Laboratories is a multimission laboratory managed and operated by National Technology & Engineering Solutions of Sandia, LLC, a wholly owned subsidiary of Honeywell International Inc., for the U.S. Department of Energy's National Nuclear Security Administration under contract DE-NA0003525. This paper describes objective technical results and analysis. Any subjective views or opinions that might be expressed in the paper do not necessarily represent the views of the U.S. Department of Energy or the United States Government.

References

Adams, M. C., Moore, J. N., Bjornstad, S., & Norman, D. I. (2000). Geologic history of the Coso geothermal system. In *Proceedings of the World Geothermal Congress; 2000/05/28; Kyushu-Tohoku, Japan. Kyushu-Tohoku, Japan. World Geothermal Congress* (pp. 205–210).

Allis, R., Blackett, B., Gwynn, M., Hardwick, C., Moore, J., Morgan, C., et al. (2012). Stratigraphic reservoirs in the Great Basin—The bridge to development of enhanced geothermal systems. *GRC Transactions*, *36*, 351–357.

Arabasz, W. J., Burlacu, R., & Pankow, K. L. (2007). An overview of historical and contemporary seismicity in central Utah. In *Central Utah—Diverse geology of a dynamic landscape* (Vol. 36, pp. 237–253). Utah Geological Association Publication.

Arabasz, W. J., Nava, S. J., McCarter, M. K., Pankow, K. L., Pechmann, J. C., Ake, J., & McGarr, A. (2005). Coal-mining seismicity and ground-shaking hazard: A case study in the Trail Mountain area, Emery County, Utah. *Bulletin of the Seismological Society of America*, *95*(1), 18–30. https://doi.org/10.1785/0120040045

Bacon, C. R., Duffield, W. A., & Nakamura, K. (1980). Distribution of Quaternary rhyolite dome of the Coso Range California: Implications for extent of the geothermal anomaly. *Journal of Geophysical Research*, *85*(B5), 2425–2433. https://doi.org/10.1029/JB085iB05p02425

Bacon, C. R., Giovannetti, D. M., Duffield, W. A., Dalrymple, G. B., & Drake, R. E. (1982). *Age of the Coso Formation Inyo County California*. U.S. Geological Survey, Washington, District of Columbia: U.S. Government Printing Office. Report No. Bulletin 1527.

Bailey, I. W., Miller, M. S., Liu, K., & Levander, A. (2012). VS and density structure beneath the Colorado Plateau constrained by gravity anomalies and joint inversions of receiver function and phase velocity data. *Journal of Geophysical Research*, *117*(2), 1–18. https://doi.org/10.1029/2011JB008522

Bensen, G. D., Ritzwoller, M. H., Barmin, M. P., Levshin, A. L., Lin, F., Moschetti, M. P., et al. (2007). Processing seismic ambient noise data to obtain reliable broad-band surface wave dispersion measurements. *Geophysical Journal International*, *169*(3), 1239–1260. https://doi.org/10.1111/j.1365-246X.2007.03374.x

Berg, E. M., Lin, F.-C., Allam, A., Qiu, H., Shen, W., & Ben-Zion, Y. (2018). Tomography of Southern California via Bayesian joint inversion of Rayleigh wave ellipticity and phase velocity from ambient noise cross-correlations. *Journal of Geophysical Research: Solid Earth*, (11), 1–17. https://doi.org/10.1029/2018JB016269

Bhattacharyya, J., & Lees, J. M. (2002). Seismicity and seismic stress in the Coso Range, Coso geothermal field, and Indian Wells Valley region, southeast-central California. *Memoir of the Geological Society of America*, *195*, 243–257. https://doi.org/10.1130/0-8137-1195-9.243

Blackwell, D., Richards, M., Frone, Z., Batir, J., Ruzo, A., Dingwall, R., & Williams, M. (2011). Temperature at depth maps for the conterminous US and geothermal resource estimates. *Geothermal Resources Council: Transactions*, *35*, 1545–1550.

Blackwell, D. D., Steele, J. L., & Carter, L. S. (1991). Heat flow patterns of the North American continent: A discussion of the DNAG geothermal map of North America. In D. B. Slemmons, E. R. Engdahl, & D. D. Blackwell (Eds.), *Neotectonics of North America, DNAG Decade Map* (Vol. 1, pp. 423–437). Geological Society of America.

Chu, R., Helmberger, D. V., Sun, D., Jackson, J. M., & Zhu, L. (2010). Mushy magma beneath Yellowstone. *Geophysical Research Letters*, *37*, L01306. https://doi.org/10.1029/2009/GL041656

Combs, J. (1980). Heat flow in the Coso geothermal area, Inyo County, California. United States. *Journal of Geophysical Research*, *85*(B5), 2411–2424. https://doi.org/10.1029/JB085iB05p02411

Coso Operating Company. (2021). Project information. Retrieved from https://cosoenergy.com/who-we-are/

Delph, J. R., Shimizu, K., & Ratschbacher, B. C. (2021). The architecture of the southern Puna magmatic system: Integrating seismic and petrologic observations with geochemical modeling. *Journal of Geophysical Research: Solid Earth*, *126*, e2020JB021550. https://doi.org/10.1029/2020JB021550

Duffield, W. A., Bacon, C. R., & Dalrymple, G. B. (1980). Late cenozoic volcanism, geochronology, and structure of the Coso range, Inyo County, California. *Journal of Geophysical Research*, *85*(B5), 2381–2404. https://doi.org/10.1029/JB085iB05p02381

Edwards, M. C., & Chapman, D. S. (2013). *A final report: Geothermal resource assessment of the Basin and Range province in western Utah: Report and heat flow map, Utah Geological Survey, Award 120000* (p. 121). U.S. Dept. of Energy Contract DE-EE0002850.

Hammond, W. C., & Humphreys, E. D. (2000). Upper mantle seismic wave velocity: Effects of realistic partial melt geometries. *Journal of Geophysical Research*, *105*(B5), 10975–10986. https://doi.org/10.1029/2000JB900041

Hardwick, C., Hurlbut, W., Gwynn, M., Allis, R., Wannamaker, P., & Moore, J. (2018). Geophysical surveys of the Milford, Utah, FORGE site: Gravity and TEM. *GRC Transaction*, *42*, 15. https://doi.org/10.34191/mp-169-f

Harmon, N., Gerstoft, P., Rychert, C. A., Abers, G. A., Salas de la Cruz, M., & Fischer, K. M. (2008). Phase velocities from seismic noise using beamforming and cross correlation in Costa Rica and Nicaragua. *Geophysical Research Letters*, *35*, L19303. https://doi.org/10.1029/2008gl035387

Heidbach, O., Tingay, M., Barth, A., Reinecker, J., Kurfeß, D., & Müller, B. (2010). Global crustal stress pattern based on the World Stress Map database release 2008. *Tectonophysics*, *462*(1–4), 3–15. https://doi.org/10.1016/j.tecto.2009.1007.1023

Holland, T., & Powell, R. (2001). Calculation of phase relations involving haplogranitic melts using an internally consistent thermodynamic dataset. *Journal of Petrology*, *42*(4), 673–683. https://doi.org/10.1093/petrology/42.4.673

IRIS Transportable Array. (2003). USArray Transportable Array [Dataset]. International Federation of Digital Seismograph Networks. https://doi.org/10.7914/SN/TA

Jia, Z., & Clayton, R. W. (2021). Determination of near surface shear-wave velocities in the central Los Angeles basin with dense arrays. *Journal of Geophysical Research: Solid Earth*, *126*(5), e2020JB021369. https://doi.org/10.1029/2020jb021369

Johnsen, R. L., Smith, E. I., & Biek, R. F. (2010). *Subalkaline volcanism in the Black Rock Desert and Markagunt Plateau volcanic fields of south-central Utah* (p. 39). Utah Geological Association Publication.

Karato, S. (1993). Importance of anelasticity in the interpretation of seismic tomography. *Geophysical Research Letters*, *20*, 1623–1626. https://doi.org/10.1029/93gl01767

Keller, G. R., Smith, R. B., & Braile, L. W. (1975). Crustal structure along the Great Basin-Colorado Plateau transition from seismic refraction studies. *Journal of Geophysical Research*, *80*(8), 1093–1098. https://doi.org/10.1029/jb080i008p01093

Knudsen, T., Kleber, E., Hiscock, A., Kirby, S. M., Allis, R., & Moore, J. N. (2019). Quaternary geology of the Utah FORGE site and vicinity, Millard and Beaver Counties, Utah. In R. Allis, & J. N. Moore (Eds.), *Geothermal characteristics of the Roosevelt Hot Springs system and adjacent FORGE EGS site*. Utah Geological Survey Miscellaneous Publication 169-B. https://doi.org/10.34191/MP-169-B

Kreemer, C., Hammond, W. C., Blewitt, G., Holland, A. A., & Bennett, R. A. (2012). A geodetic strain rate model for the Pacific-North American plate boundary, western United States. In *Nevada Bureau of Mines and Geology Map 178, Scale 1:1,500,000*.

Larsen, E. S. (1929). The temperatures of magmas. *American Mineralogist*, *14*, 81–94.

Lin, F. C., Li, D., Clayton, R. W., & Hollis, D. (2013). High-resolution 3D shallow crustal structure in Long Beach, California: Application of ambient noise tomography on a dense seismic array. *Geophysics*, *78*(4), Q45–Q56. https://doi.org/10.1190/geo2012-0453.1

Lin, F. C., Moschetti, M. P., & Ritzwoller, M. H. (2008). Surface wave tomography of the western United States from ambient seismic noise: Rayleigh and Love wave phase velocity maps. *Geophysical Journal International*, *173*(1), 281–298. https://doi.org/10.1111/j.1365-246X.2008.03720

Lin, F. C., Ritzwoller, M. H., & Snieder, R. (2009). Eikonal tomography: Surface wave tomography by phase front tracking across a regional broad-band seismic array. *Geophysical Journal International*, *177*(3), 1091–1110. https://doi.org/10.1111/j.1365-246X.2009.04105.x

Lin, F.-C., & Schmandt, B. (2014). Upper crustal azimuthal anisotropy across the contiguous U.S. determined by Rayleigh wave ellipticity. *Geophysical Research Letters*, *41*, 8301–8307. https://doi.org/10.1002/2014GL062362

Lin, F. C., Schmandt, B., & Tsai, V. C. (2012). Joint inversion of Rayleigh wave phase velocity and ellipticity using USArray: Constraining velocity and density structure in the upper crust. *Geophysical Research Letters*, *39*(12), 1–7. https://doi.org/10.1029/2012GL052196

Lin, F.-C., Tsai, V. C., & Schmandt, B. (2014). 3-D crustal structure of the western United States: Application of Rayleigh-wave ellipticity extracted from noise cross-correlations. *Geophysical Journal International*, *198*(2), 656–670. https://doi.org/10.1093/gji/ggu160

Lowell, R. P., Cappellen, P. V., & Germanovich, L. N. (1993). Silica precipitation in fractures and the evolution of permeability in hydrothermal upflow zones. *American Association for the Advancement of Science*, *260*(5105), 192–194. https://doi.org/10.1126/science.260.5105.19

McClusky, S. C., Bjornstad, S. C., Hager, B. H., King, R. W., Meade, B. J., Miller, M. M., et al. (2001). Present day kinematics of the eastern California shear zone from a geodetically constrained block model. *Geophysical Research Letters*, *28*(17), 3369–3372. https://doi.org/10.1029/2001GL013091

Mesimeri, M., Pankow, K. L., Baker, B., & Hale, J. M. (2021). Episodic earthquake swarms in the Mineral Mountains, Utah driven by the Roosevelt hydrothermal system. *Journal of Geophysical Research: Solid Earth*, *126*, e2021JB021659. https://doi.org/10.1029/2021JB021659

Mesimeri, M., Pankow, K. L., Barnhart, W. D., Whidden, K. M., & Hale, J. M. (2021). Unusual seismic signals in the Sevier Desert, Utah possibly related to the Black Rock volcanic field. *Geophysical Research Letter*. https://doi.org/10.1029/2020GL090949

Monastero, F. C. (2002). An overview of Industry–Military cooperation in the development of power operations at the Coso geothermal field in southern California. *GRC Bulletin*, *188*, 194.

Monastero, F. C., Katzenstein, A., Miller, J., Unruh, J. R., Adams, M., & Richards-Dinger, K. (2005). The Coso geothermal field: A nascent metamorphic core complex. *The Geological Society of America Bulletin*, *117*(11), 1534–1553. https://doi.org/10.1130/B25600.1

Moore, J., McLennan, J., Pankow, K., Simmons, S., Podgorney, R., Wannamaker, P., et al. (2020). The Utah frontier observatory for research in geothermal energy (FORGE): A laboratory for characterizing, creating, and sustaining enhanced geothermal systems. In *Proceedings of the 45th Workshop on Geothermal Reservoir Engineering*. Stanford University.

Moschetti, M., Ritzwoller, M., Lin, F., & Yang, Y. (2010a). Seismic evidence for widespread western-US deep-crustal deformation caused by extension. *Nature*, *464*, 885–889. https://doi.org/10.1038/nature08951

Moschetti, M. P., Ritzwoller, M. H., Lin, F.-C., & Yang, Y. (2010b). Crustal shear wave velocity structure of the western United States inferred from ambient seismic noise and earthquake data. *Journal of Geophysical Research*, *115*, B10306. https://doi.org/10.1029/2010JB007448

Mosegaard, K., & Tarantola, A. (1995). Monte Carlo sampling of solutions to inverse problems. *Journal of Geophysical Research*, *100*(B7), 12431–12447. https://doi.org/10.1029/94JB03097

Muller, G., & Mueller, S. (1979). Travel-time and amplitude interpretation of crustal phases on the refraction profile Delta-W, Utah. *Bulletin of the Seismological Society of America*, *69*(4), 1121–1132.

Nevada Department of Minerals (2021). Nevada geothermal production summary 2020. Retrieved from https://minerals.nv.gov/Programs/Geo/Geo/

Olson, T. L., & Smith, R. B. (1976). Earthquake surveys of Roosevelt Hot Springs and the Cove Fort areas, Utah, M.S. Thesis. M.S. Thesis. University of Utah, Salt Lake City, Utah (p. 80).

Özalaybey, S., Savage, M. K., Sheehan, A. F., Louie, J. N., & Brune, J. N. (1997). Shear-wave velocity structure in the northern Basin and Range province from the combined analysis of receiver functions and surface waves. *Bulletin of the Seismological Society of America*, *87*(1), 183–199. https://doi.org/10.1785/BSSA0870010183

Pankow, K. (2016). FORGE nodal array 1 [Data set]. International Federation of Digital Seismograph Networks. https://doi.org/10.7914/SN/8J_2016

Poletto, F., Farina, B., & Carcione, J. (2018). Sensitivity of seismic properties to temperature variations in a geothermal reservoir. *Geothermics*, *76*, 149–163. https://doi.org/10.1016/j.geothermics.2018.07.001

Robinson, R., & Iyer, H. M. (1981). Delineation of a low-velocity body under the Roosevelt Hot Springs geothermal area, Utah, using teleseismic P-wave data. *Geophysics*, *46*(10), 1456–1466.

Roux, P., & Ben-Zion, Y. (2017). Rayleigh phase velocities in Southern California from beamforming short-duration ambient noise. *Geophysical Journal International*, *211*(1), 450–454. https://doi.org/10.1093/gji/ggx316

Rowley, P. D., Rutledge, E. F., Maxwell, D. J., Dixon, G. L., & Wallace, C. A. (2013). *Geology of the Sulphurdale geothermal-resource area, Beaver and Millard counties, Utah* (Vol. 609, p. 33). Utah Geological Survey, Open-File Report.

Saishu, H., Okamoto, A., & Tsuchiya, N. (2014). The significance of silica precipitation on the formation of the permeable-impermeable boundary within Earth's crust. *Terra Nova*, *26*(4), 253–259. https://doi.org/10.1111/ter.12093

Schmandt, B., & Humphreys, E. (2010). Complex subduction and small-scale convection revealed by body-wave tomography of the western United States upper mantle. *Earth and Planetary Science Letters*, *297*(3–4), 435–445. https://doi.org/10.1016/j.epsl.2010.06.047

Shapiro, N. M., Campillo, M., Stehly, L., & Ritzwoller, M. H. (2005). High-resolution surface wave tomography from ambient seismic noise. *Science*, *307*, 1615–1618. https://doi.org/10.1126/science.1108339

Shen, W., Ritzwoller, M. H., Schulte-Pelkum, V., & Lin, F. C. (2012). Joint inversion of surface wave dispersion and receiver functions: A bayesian Monte-Carlo approach. *Geophysical Journal International*, *192*(2), 807–836. https://doi.org/10.1093/gji/ggs050

Simmons, S. F., Moore, J., Allis, R., Kirby, S., Jones, C., Bartley, J., et al. (2018). A revised geoscientific model for FORGE Utah EGS Laboratory. In *Proceedings of the 43rd Workshop on Geothermal Reservoir Engineering* (pp. 1–8).

Sine, C. R., Wilson, D., Gao, W., Grand, S. P., Aster, R., Ni, J., & Baldridge, W. S. (2008). Mantle structure beneath the western edge of the Colorado Plateau. *Geophysical Research Letters*, *35*(10), 1–5. https://doi.org/10.1029/2008GL033391

Smith, R. B., & Arabasz, W. J. (1991). Seismicity of the Intermountain seismic belt. In D. B. Slemmons, E. R. Engdahl, M. D. Zoback, & D. D. Blackwell (Eds.), *Neotectonics of North America, decade map* (Vol. 1). Geophysical Society of America.

Smith, R. B., Braile, L. W., & Keller, G. R. (1975). Upper crustal low-velocity layers: Possible effect of high temperatures over a mantle upwarp at the Basin Range—Colorado Plateau transition. *Earth and Planetary Science Letters*, *28*(1), 197–204.

Tanimoto, T., & Rivera, L. (2008). The ZH ratio method for long-period seismic data: Sensitivity kernels and observational techniques. *Geophysical Journal International*, *172*(1), 187–198. https://doi.org/10.1111/j.1365-246X.2007.03609.x

Traer, J., Gerstoft, P., Bromirski, P., & Shearer, P. (2012). Microseisms and hum from ocean surface gravity waves. *Journal of Geophysical Research*, *117*, B11307. https://doi.org/10.1029/2012JB009550

Trow, A. J., Zhang, H., Record, A. S., Mendoza, K. A., Pankow, K. L., & Wannamaker, P. E. (2018). Microseismic event detection using multiple geophone arrays in Southwestern Utah. *Seismological Research Letters*, *89*(5), 1660–1670. https://doi.org/10.1785/0220180065

University of Nevada, Reno. (1971). Nevada seismic network [Data set]. International Federation of Digital Seismograph Networks. https://doi.org/10.7914/SN/NN

University of Utah. (1962). University of Utah regional seismic network [Data set]. International Federation of Digital Seismograph Networks. https://doi.org/10.7914/SN/UU

Wang, Y., Lin, F. C., & Ward, K. M. (2019). Ambient noise tomography across the Cascadia subduction zone using dense linear seismic arrays and double beamforming. *Geophysical Journal International*, *217*(3), 1668–1680. https://doi.org/10.1093/gji/ggz109

Wannamaker, P. E., Bartley, J. M., Sheehan, A. F., Jones, C. H., Lowry, A. R., Dumitru, T. A., et al. (2001). Great Basin-Colorado Plateau transition in central Utah: An interface between active extension and stable interior. *Utah Geological Association Publication*, *30*, 1–38. http://129.123.73.40/~arlowry/Papers/GBCP_UGA.pdf

Wannamaker, P. E., Hasterok, D. P., Johnston, J. M., Stodt, J. A., Hall, D. B., Sodergren, T. L., et al. (2008). Lithospheric dismemberment and magmatic processes of the Great Basin-Colorado Plateau transition, Utah, implied from magnetotellurics. *Geochemistry, Geophysics, Geosystems*, *9*(5), 1–38. https://doi.org/10.1029/2007GC001886

Wannamaker, P. E., Simmons, S. F., Miller, J. J., Hardwick, C. L., Erickson, B. A., Bowman, S. D., et al. (2020). Geophysical Activities over the Utah FORGE site at the outset of Project Phase 3. In *Proceedings of the 45th Workshop on Geothermal Reservoir Engineering Stanford University* (pp. 1–14).

Wu, H., & Lees, J. M. (1999). Three-dimensional P and S waves velocity structures of the Coso geothermal area, California, from microseismic travel time data. *Journal of Geophysical Research*, *104*(5), 13217–13233.

Yang, Y., Ritzwoller, M. H., & Jones, C. H. (2011). Crustal structure determined from ambient noise tomography near the magmatic centers of the Coso region, southeastern California. *Geochemistry, Geophysics, Geosystems*, *12*(2), 1–20. https://doi.org/10.1029/2010GC003362